

voFoam – A geometrical Volume of Fluid algorithm on arbitrary unstructured meshes with local dynamic adaptive mesh refinement using OpenFOAM

Tomislav Marić, Holger Marschall, and Dieter Bothe

ABSTRACT. A new parallelized unsplit geometrical Volume of Fluid (VoF) algorithm with support for arbitrary unstructured meshes and dynamic local Adaptive Mesh Refinement (AMR), as well as for two and three dimensional computation is developed. The geometrical VoF algorithm supports arbitrary unstructured meshes in order to enable computations involving flow domains of arbitrary geometrical complexity. The implementation of the method is done within the framework of the OpenFOAM library for Computational Continuum Mechanics (CCM) using the C++ programming language with modern policy based design for high program code modularity. The development of the geometrical VoF algorithm significantly extends the method base of the OpenFOAM library by geometrical volumetric flux computation for two-phase flow simulations.

For the volume fraction advection, a novel unsplit geometrical algorithm is developed, which inherently sustains volume conservation utilizing unique Lagrangian discrete trajectories located in the mesh points. This practice completely eliminates the possibility of an overlap between the flux polyhedra and hence significantly increases volume conservation. A new efficient (quadratic convergent) and accurate iterative flux correction algorithm is developed, which avoids topological changes of the flux polyhedra. Our geometrical VoF algorithm is dimension agnostic, providing automatic support for both 2D and 3D computations, following the established practice in OpenFOAM. The geometrical algorithm used for the volume fraction transport has been extended to support dynamic local AMR available in OpenFOAM. Furthermore, the existing dynamic mesh capability of OpenFOAM has been modified to support the geometrical mapping algorithm executed as a part of the dynamic local AMR cycle. The method implementation is fully parallelized using the domain decomposition approach.

The majority of the standard established test cases for verification and validation of VoF algorithms has been thoroughly tested with varying Courant numbers. Our results for the first time show a VoF algorithm on unstructured meshes to be robust, mass conservative and boundedness-preserving for complex time-varying velocity fields. The obtained volume of symmetric difference interface reconstruction errors are the lowest reported so far in the literature for unstructured meshes.

1. Introduction

The *geometrical* Volume-of-Fluid (VoF) method is a method where the interface is represented by a set of simple geometrical entities and advection of the volume fraction is accomplished using geometrical algorithms. When the interface is represented as a set of polygons (planes) reconstructed from the volume fraction field, the geometrical VoF algorithm is commonly known as the Piecewise Linear Interface Calculation (PLIC) algorithm (DeBar, 1974; Rider and Kothe, 1998). Geometrical operations involving interface planes and mesh cells are then performed in order to advect the volume fraction field.

The widespread use of the geometrical Volume of Fluid (VoF) method for simulating two-phase flow is mostly based on its intrinsic mass conservation and the ability to automatically deal with topological changes of the fluid interface (no special operations on the discrete interface geometry are required). However, the majority of the developments related to the geometrical VoF method have so far been done on Cartesian and structured meshes because of the high numerical accuracy they provide and the simplicity of the algorithms relying on structured mesh points. Problems involving complex geometrical shapes of the flow domain, usually rely on automatic (fast) algorithms for generation of unstructured meshes. For this reason, the use of unstructured meshes has prevailed in those parts of the industry and research where complex geometry of the flow domain is of importance. However, the use of an accurate geometrical VoF method for such problems was not possible so far; instead VoF methods involving algebraic advection of the volume fraction field are in widespread use.

1991 *Mathematics Subject Classification.* flu-dyn.

Key words and phrases. volume of fluid method, unstructured mesh, geometrical advection, adaptive mesh refinement, OpenFOAM .

The authors hereby gratefully acknowledge the financial support by the German Research Foundation (DFG) and the German Council of Science and Humanities, in the framework of the DFG Cluster of Excellence EXC 259.

This contribution utilises the OpenFOAM[®] software for Computational Continuum Mechanics (CCM) as an implementation platform for the geometrical VoF method on arbitrary unstructured meshes. As detailed in the following, the developed geometrical VoF method is based on novel a directionally unsplit advection algorithm using a full discrete Lagrangian flow map on unstructured meshes and thus allowing for accurate direct numerical simulation (DNS) of two-phase flow in domains of arbitrary geometrical complexity. The geometrical VoF algorithm for volume fraction transport is shown to be robust, volume conservative and boundedness preserving; it is fully parallelized using the domain decomposition approach and supports dynamic local Adaptive Mesh Refinement (AMR). The algorithm utilizes a new efficient (quadratic convergent) and accurate iterative flux correction algorithm, that avoids topological changes of the flux polyhedra and inherently ensures mass conservation. To the best of the authors' knowledge, for the first time such a geometrical VoF method is shown to be capable to deal with three dimensional, spatially complex and time varying velocity fields. The obtained volume of symmetric difference interface reconstruction errors are the lowest reported so far in the literature for unstructured meshes. The development of the geometrical VoF algorithm significantly extends the method base of the OpenFOAM library using a modern policy based design for high program code modularity and combinatorial complexity of sub-algorithms for geometrical reconstruction and advection.

OpenFOAM is a Finite Volume Method (FVM) library for Computational Continuum Mechanics (CCM) written in the C++ programming language. It has a modular structure and provides a possibility of an extensive re-use of the available functionality. A broad choice of mathematical and constitutive models is available, as well as linear solvers, dynamic mesh operations involving both mesh motion and topological operations and a comprehensive set of boundary conditions, etc. Details of the development model of OpenFOAM and its relationship to continuum mechanical modeling and simulations of CCM problems are provided by Weller et al. (1998) and Jasak et al. (2007). The benefit of developing the geometrical VoF method for unstructured meshes using OpenFOAM within an *Open Source* framework is thus two-fold: it provides an implementation with the ability to deal with arbitrarily complex flow domains, and it allows for extensions of the method by coupling with the present functionality of the OpenFOAM library.

The goal of this work is to develop a geometrical VoF library and a set of solver applications that can deal with two-phase flows involving complex transport processes (*complex flows*) in complex domains (*complex geometry*). The topology of an unstructured meshes dictates our choice of algorithms for both the reconstruction of the interface geometry and the advection of the volume fraction, as well as the underlying geometrical operations. The fluid interface is approximated with a piecewise planar geometry which is reconstructed using the method of Parker and Youngs (1992) with an alternative accurate parallelized gradient calculation on arbitrary unstructured mesh and is able to deal with arbitrary shapes of the mesh cells. An Eulerian unsplit geometrical algorithm is chosen for the volume fraction advection, based on a full unique Lagrangian trajectories located in the cell corner points. We do not consider complicated geometrical operations necessary for non-convex congruent polyhedra, which may be constructed by the advection algorithm in those parts of the flow domain where insufficient resolution is provided. The reason for this decision is that the flow will be sufficiently resolved by local dynamic AMR near the interface.

The accuracy of the geometrical VoF method can be enhanced when coupled with dynamic local Adaptive Mesh Refinement (AMR)¹ (see Kothe et al. (1996) and Černe et al. (2002) for details). Extensions to higher order geometrical methods such as the Moment-of-Fluid (MoF) method of Ahn and Shashkov (2009) or higher order reconstruction (e.g. Patterned Interface Reconstruction by Mosso et al. (2009)) are also possible if it proven to be necessary (even with applied AMR).

1.1. State of the art. For the sake of clarity, we provide a brief overview of the important aspects of the geometrical VoF method as well as the related terminology. Emphasis is put upon geometrical VoF methods and related algorithms rather than the algebraic VoF method. The interested reader is referred to appropriate references in literature once the scope of this overview is left.

In order to advect the volume fraction field using geometrical algorithms, the geometrical representation of the interface needs to be sufficiently accurate, and the geometrical advection algorithm must conserve mass as well as avoid artificial deformation of the interface, while keeping the volume fraction field bounded between values of 0 and 1.

Since the interface is described as a set of planes (polygons) the orientation of which is given by the volume fraction field, the planes are disconnected on cell faces. Discontinuities of the interface planes at cell faces may be described in terms of *geometrical stability* of the interface. The discontinuities decrease with the increase of mesh resolution and the accuracy of the gradient calculation, used to determine the orientation of the plane normals. Furthermore, the orientations of the interface planes may be additionally optimized in a way that does not impose errors in mass conservation. Such second order convergent reconstruction

¹From this point on in the text, dynamic local AMR will be referred to as AMR since it must follow an evolving fluid interface when applied to two-phase flow simulations.

algorithms² result in smaller discontinuities, but involve additional computational complexity. However, it is of utmost importance to reduce them to a minimum, since geometrical instabilities generated by the reconstruction algorithm cause accumulation of other errors during the advection of the volume fraction field (Černe et al., 2002).

Geometrical advection algorithms may be sorted into two general categories based on the direction splitting: directional (operator) split and un-split algorithms. Another division may be defined based on the choice of the mesh geometry used to advect the volume fraction field: *face swept*, and *Lagrangian re-mapping* algorithms.

Operator split algorithms compute the volume fraction fluxes interchangeably in directions orthogonal to the coordinate axes. Such ordering is native to a structured mesh, but can be extracted from the unstructured hexahedral mesh as well. Since the advection directions are interchanged, each advection iteration is followed by a reconstruction step where the interface geometry is computed from the updated volume fraction field.

Directional un-split algorithms compute the advection of the volume fraction field in a single computational step, using the velocity vectors. Hence, a single reconstruction of the interface is required after each advection step.

Face-swept algorithms rely on flux calculations coming from sweeping or *back-tracing* cell faces along the streamlines given by the velocity field. A *swept polyhedron* is then adjusted, such that its volume equals the value of the volumetric flux coming from the numerical solution of the pressure equation in order to assure mass conservation.

Eulerian backtracking / Lagrangian re-mapping algorithms compute the increase of the volume fraction on a per-cell basis, by sweeping the mesh backward using the velocity field interpolated to the mesh vertices, and intersecting the swept mesh with the geometrical data of the interface. After this Lagrangian backtracking step, a re-mapping is executed on the underlying Eulerian mesh to set the new volume fraction values.

On unstructured meshes, both face-swept and Lagrangian-Eulerian re-mapping algorithms are directionally un-split. Depending on the complexity of the flow field, both face-swept and Lagrangian re-mapping algorithms encounter problems in geometrical operations because the created polyhedra have non-planar faces and may even be non-convex.

A detailed review of algorithms involving two-phase flow methods on structured meshes with emphasis on the geometrical VoF method can be found in a book on Direct Numerical Simulations (DNS) of two-phase flows by Tryggvason, Scardovelli, and Zaleski (2011) and in journal contributions by Rider and Kothe (1998), Scardovelli and Zaleski (1999), Scardovelli and Zaleski (2003), and Aulisa et al. (2007). For latest developments on Cartesian structured meshes the interested reader is referred to (Weymouth and Yue, 2010; Mencinger and Žun, 2011; Chenadec and Pitsch, 2013) and the references therein. A detailed numerical analysis of the errors native to the two-dimensional geometrical VoF method on structured meshes is described in Černe et al. (2002). So far, main contributions to geometrical algorithms for VoF methods were concentrated on the following aspects: improving interface normal orientation, improving overall mass conservation, reducing under-and-overshoots of the volume fraction, and removing wisps and artificial interface separation.

In the remainder we present a brief overview of the research efforts involving three-dimensional calculations and geometrical VoF algorithms which support *unstructured* domain discretization, since they are more relevant to our work.

Mosso et al. (1996) and Kothe et al. (1996) have produced first (to our knowledge) publications referring to a geometrical VoF method with support for unstructured meshes.

Kothe et al. (1996) emphasize that the motivation behind research towards unstructured meshes is based on the requirement for arbitrary geometrical complexity of the flow domain. Important aspects of the gradient reconstruction for the volume fraction field is presented, resulting in a conclusion that a wide cell stencil (27 cells for a hexahedral mesh) is necessary in order to obtain geometrical stability of the reconstructed interface. A valuable note is provided regarding the visualization of results, which emphasizes the importance of viewing the actual polygonal geometry of the reconstructed interface. Standard visualization practice utilises an iso-surface representation of the interface, where the iso-value of the volume fraction is prescribed (e.g. to a value of 0.5). However, the use of iso-contours for visualizing interfaces introduces artificial connectivity of the interface e.g. for thin filaments. Besides this, the iso-contour hides all the errors which are shown when the polygonal geometry is used to visualize the interface: *wisps* – small differences in the volume fraction in the bulk of the phases from values 0 or 1 that cause reconstructed interface geometry to appear (cp. Harvie and Fletcher (2000) for details) – or even larger artificially separated parts of the interface may not be shown.

²Order of convergence of geometrical algorithms is related to convergence of standard geometrical reconstruction or advection errors.

Mosso et al. (1996) developed a second order convergent interface reconstruction method for unstructured meshes. The reconstruction is based on optimizing the orientation of the plane normals taking into account orientation of the planes in the neighbouring interface cells. For the advection of the volume fraction, a full Lagrangian back tracing of the finite volume mesh is performed, followed by a geometrical intersection with the PLIC geometry, and remapping of the volume fraction field onto the Eulerian background mesh. This advection algorithm is directionally un-split, it relies completely on the discrete flow map and requires a single reconstruction step per advection iteration.

Kothe et al. (1999) provides an overview of the geometrical VoF method developed for simulating metal casting processes in complex molds. Although a casting process is a specialized application of the geometrical VoF method, the problems involving the complex domain geometry and physical characteristics of the model (e.g. significant differences in values of physical properties across the interface), make the requirements applicable to a general purpose geometrical VoF method. They show preliminary results involving reconstruction of an interface on an unstructured tetrahedral mesh.

Ahn and Shashkov (2008) present geometrical algorithms used for the reconstruction and advection step operations, with support for polyhedral cells. They report successful three-dimensional reconstructions of complex geometrical shapes using the method of Parker and Youngs (1992) and the Least-squares-Volume-of-fluid-Interface-Reconstruction-Algorithm (LVIRA) developed by Puckett (1991), both modified in order to support polyhedral cell shapes. Dyadechko and Shashkov (2005) present three dimensional results of the Moment of Fluid (MoF) reconstruction method which optimizes the difference in position of the barycentric centre of the truncated polyhedron filled with a specific phase. The MoF method can be viewed as an extension of the geometrical VoF method by introducing additional information in the form of barycentric centres of the truncated cells, which results in a more accurate reconstruction algorithm (see Ahn and Shashkov (2007) for details on multi-material reconstruction on polyhedral meshes).

Jófre et al. (2010) show three-dimensional results for both geometrical reconstruction and the volume fraction advection on unstructured finite volume mesh. The authors present the volume fraction evolution for rotational flow using a full discrete Lagrangian flow map. Obtained errors of the advection algorithm are close in magnitude to those reported by other authors on structured meshes (see Liović et al. (2006) and Hernández et al. (2008)).

Mosso et al. (2009) developed the geometrical reconstruction algorithm called Patterned Interface Reconstruction (PIR) algorithm. The algorithm is of second order of convergence (reconstructs planes exactly) on tetrahedral (and triangular) meshes. The interface geometry is initially reconstructed using the Youngs PLIC reconstruction algorithm followed by linear or spherical smoothing operations based on the geometrical pattern formed by a group of interface polygons. Apart from reconstruction algorithm of the MoF method, this is the only reconstruction algorithm of second order that directly applies to arbitrary unstructured meshes.

Liović et al. (2006) have developed a three-dimensional extension of the original algorithm of Rider and Kothe on Cartesian meshes with a new accurate reconstruction algorithm and an elegant flux divergence correction method used for improving the mass conservation. Errors in mass conservation appear because of overlaps between the flux polyhedra on common mesh edges. Although the algorithm shows good results, it relies on a directed connectivity between cells (e.g. *L-shaped stencils*) that requires the use of a structured mesh. Additional computation of directed cell connectivity would be possible for unstructured *hexahedral* meshes, but not on arbitrary unstructured meshes.

López et al. (2004) show results with a full discrete flow map as a source for the back tracing of the flux polyhedra on a two-dimensional Cartesian mesh. Local geometrical corrections of the flux polyhedron are applied in order to ensure mass conservation. For the reconstruction algorithm, a compact spline reconstruction algorithm, with splines based on the centre points of the reconstructed interface line segments is used. This work is extended to three dimensions, again on a Cartesian mesh, by Hernández et al. (2008) and López et al. (2008). However, the construction of swept polyhedra is based on edge centres of the Cartesian mesh, with velocities interpolated from the staggered velocity field mapped to the face centres. Although a notable improvement is achieved, there is still a possibility of an overlap between the flux polyhedra around face corners. However, the mass conservation is strictly met by an analytical approach to adjusting the swept polyhedron volume.

Ivey and Moin (2012) have implemented the so-called edge-matched flux polyhedra algorithm in 3D (EMFPA 3D), suggested as an improvement of the unsplit VoF algorithm developed by Hernández et al. (2008). The algorithm locally approximates a stream tube emanating from the flux face. The flux face is triangulated to construct the flux polyhedron, which then is modified to correct the non-planarity of the faces. Divergence correction, as recommended by Hernández et al. (2008), relies on an analytical expression for computing the volumes of convex polyhedrons. Adjusting the flux polyhedron introduces overlapping of the flux polyhedra that needs to be further corrected to prevent the volume fraction from over-/undershooting.

Unfortunately, a validation of the results showing quantitative information on the standard advection errors are not provided.

Summarizing, all of the aforementioned algorithms rely on *divergence corrections* in some form to account for the fact that the discrete velocity field used for the construction of the flux polyhedron is not divergence free. Besides this issue, wisps (see Harvie and Fletcher (2000) for details) are present in the volume fraction field, and are subsequently redistributed.

As for AMR, Popinet (2003) developed a very advanced geometrical VoF method that supports both 2D and 3D calculations with AMR on structured mesh. The domain discretization is based on an *octree* data structure which enables fast and flexible mesh refinement operations and locally accurate differentiation. Recently, Popinet (2009) has shown that the AMR plays a significant role in reducing *parasitic currents*. Details on the capabilities and applications of the octree based geometrical VoF method are provided by Fuster et al. (2009) and Agbaglah et al. (2011).

Fully unstructured AMR available in OpenFOAM delegates the refinement to each cell, and is hence able to deal in a straightforward way with arbitrary cell shapes and solution domains of arbitrary geometrical complexity. With fully unstructured AMR, a new mesh is created with refined and unrefined regions each time a topological operation is executed. The octree based AMR implies a flow domain in the shape of a regular hexahedron.

We have chosen the fully unstructured AMR since it does not restrict us to a specific cell shape (allows automatic mesh generation of complex solution domains) and it is already a part of the OpenFOAM library, which means it can be coupled to other dynamic mesh functionality (mesh motion, mesh deformation, sliding interfaces, moving reference frames, etc.).

In the following section the governing equations of the flow are described. Geometrical operations required by the unstructured meshes and their use in the reconstruction and advection step of the method are presented in the third section. In the fourth section the coupling between the numerical solution of the governing equations and the geometrical evolution of the volume fraction is set out. Results and discussions are presented in the two final sections.

2. Geometrical evolution of the volume fraction field

The advection equation for the volume fraction field of a phase α for an incompressible flow is written in the following form:

$$(2.1) \quad \partial_t \alpha + \nabla \cdot (\mathbf{U} \alpha) = 0.$$

Applying the discretization practice of the unstructured FVM, with the first order Euler explicit time discretization on Equation 2.1, results with the following algebraic equation:

$$(2.2) \quad \alpha_c^n = \alpha_c^o - \frac{\Delta t}{V_c} \sum_f \alpha_f \mathbf{U}_f \cdot \mathbf{S}_f,$$

where f denotes the face of a computational cell (cp. Fig. 1) and, correspondingly, \mathbf{U}_f and \mathbf{S}_f are the face-centered velocity and face area normal vectors shown in Figure 1.

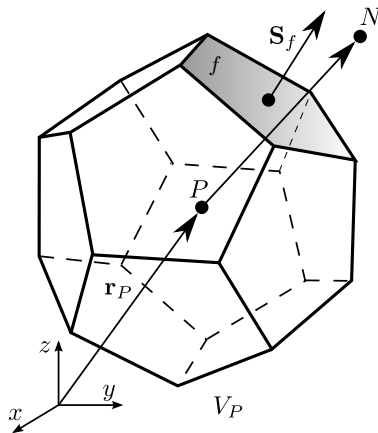


Figure 1. Polyhedral cell.

The unstructured FVM utilises a computational domain decomposed into non-overlapping convex polyhedra (Figure 1) which are the building elements of the unstructured mesh. However, the implementation

of the mesh is done in an efficient way, when it comes to addressing the information needed by numerical algorithms. More precisely, the mesh points are defined only once as a set of position vectors, and are indirectly addressed by the unstructured FVM algorithms. The indirect addressing leads to the definitions of faces and cells as sets of indirect indices: the face is thus an ordered set of indices which relate (map) to the list of mesh points, and the mesh cell is a set of indices which relate to the list of mesh faces.

The ordering of the face indices determines the orientation of the face area normal vector \mathbf{S}_f , shown in Figure 1. For the polyhedron in Figure 1, the cell index in the list of mesh cells is lower than the cell index of its neighbour across the face f . This makes the polyhedron the *owner* of the face f , and makes the ordering of the indices of the face f such that the face area normal vector \mathbf{S}_f points outwards from the owner polyhedron, and into the neighbor polyhedron. Such ordering allows for efficient (unique) computation of the volumetric fluxes used by unstructured FVM.

An algebraic approach to solving Equation 2.2 utilizes bounded higher-order interface capturing (compressive) advection schemes on unstructured meshes to determine the face-centered volume fraction value α_f . This practice often results in an artificial smearing of the volume fraction field as well as artificial deformation of the interface.

The geometrical VoF algorithm solves Equation 2.2 by computing the fluxed phase volume:

$$(2.3) \quad V_{f,\alpha} = \alpha_f \|\mathbf{U}_f \cdot \mathbf{S}\| \Delta t = \alpha_f \|F_f\| \Delta t$$

using geometrical operations, where F_f is the volumetric flux across the face f with an outward pointing surface area normal vector \mathbf{S} (\mathbf{S}_f for a computational cell formally owning the face f – cf. Figure 1), which satisfies the discrete divergence free condition:

$$(2.4) \quad \sum_f F_f = 0.$$

Without the indirect addressing of the unstructured mesh, (2.4) would be computed on a per-cell basis, repeating the flux calculation twice per cell face. To avoid this, the flux is computed using the oriented face area normal vector \mathbf{S}_f and the owner-neighbor addressing of the unstructured mesh:

$$(2.5) \quad \sum_f \alpha_f \mathbf{U}_f \cdot \mathbf{S} = \sum_{\text{owner}} \alpha_f \mathbf{U}_f \cdot \mathbf{S}_f - \sum_{\text{neighbor}} \alpha_f \mathbf{U}_f \cdot \mathbf{S}_f,$$

thus computing the same flux once per cell and adding the flux contribution to the owner cell (outward directed \mathbf{S}_f) and deducting the flux contribution from the neighbor cell (inward directed \mathbf{S}_f).

Because of the geometrical multidimensionality of the directionally unsplit advection algorithm, the artificial deformation of the interface which is transported in the *skew direction*³ is significantly reduced, compared to fluxed-based methods based on algebraic differencing schemes. Such geometrical way of computing the fluxed phase volume also ensures the interface geometry to remain located within a single layer of cells throughout the simulation which is consistent with the discrete counter-part of the underlying sharp interface model.

The geometrical VoF method relies on geometrical information of the interface. In our work, we have used a standard approach for the geometrical VoF algorithm: a planar geometry of the interface is placed within an *interface cell* and the geometrical evolution of the volume fraction field is performed by two subsequent steps, namely the *interface reconstruction* and the *volume fraction advection* step. This algorithm is commonly known as Piecewise Linear Interface Calculation (PLIC) algorithm (Rider and Kothe, 1998).

In the remainder we provide a detailed explanation of the supporting geometrical operations and both geometrical steps of our geometrical VoF method.

2.1. Basic geometrical operations. Two geometrical operations are the basis for both the reconstruction and the advection step: the intersection between a plane and a polyhedron, and the intersection between two polyhedrons. These operations belong to the field of *Computational Geometry* (Schneider and Eberly, 2002; De Berg et al., 2008) and are usually sources of difficulties when it comes to calculations that support geometrical advection of the volume fraction in three dimensions. The reason for this lies in the fact that the polyhedrons involved in the intersection operations become non-convex due to the local complexity of the discrete velocity field. When the full Lagrangian discrete flow map is used to compute the flux polyhedrons, complex flow fields may introduce non planarity of the swept faces. As reported by Ahn and Shashkov (2009), in case of a full Lagrangian backtracking of the whole mesh, and subsequent re-mapping onto the Eulerian static mesh, the faces of the swept cells may be non-planar, and the resulting polyhedrons non-convex. If this occurs, a simplification of the swept mesh is performed that enforces geometrical operations on convex polyhedrons for the sake of simplicity and robustness of the overall algorithm.

Intersection between a plane and a convex polyhedron is calculated using the *polyhedron clipping and capping algorithm*, using a slightly modified version of the algorithm described by Ahn and Shashkov (2008).

³Skew direction in the mesh is the direction of the point or edge neighbor cells.

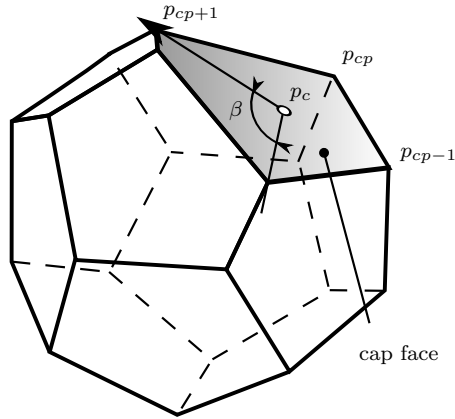


Figure 2. Cutting (clipping and capping) of a polyhedral cell.

As the method’s name suggests, each face of the polyhedron is visited and *clipped* by a plane, marking the new vertices that will at the end be added as the polyhedron *cap face*. Once all the faces are clipped, the capping algorithm will append the final cap face making sure there are no repeated points. The polyhedron faces are defined to be oriented counter clockwise, when viewed from outside of the polyhedron. Special cases may appear during the geometrical operation, which may result in an intersection being represented as: void, point, edge, face or the complete polyhedron. All these cases are internally and automatically dealt with within the clipping part of the algorithm implementation.

The final cap face of the polyhedron is shown in Figure 2. The order of the cap vertices p_{cp} could be computed using the connectivity of the clipped polyhedron: cap vertices belong to edges that have only a single face attached to them after the clipping part of the algorithm is finished. In Figure 2, cp marks the cap point and p_c is the center point of the cap. However, we have sorted the points based on the angle the vertex makes with respect to the cap center axis, given by the first cap point candidate. Since we are dealing with polyhedra that have small number of faces (finite volume cells usually have a small number of faces), an angle based insertion sort is less complicated to implement and is efficient when compared to constructing the face connectivity information to locate cap edges of the polyhedron using a graph representation of the polyhedron. In order to find the cap edges using edge-face connectivity, an edge based graph representation of the polyhedron would be necessary. Once the clipping and capping of the polyhedron is performed, the intersection between the polyhedron and a plane is complete.

The intersection between two convex polyhedrons can be built by applying the polyhedron clipping and capping algorithm for each face of a polyhedron. The same algorithm is used for calculating the intersection between a plane and a cell, additionally ensuring the face normal is directed outwards from the polyhedron created from the mesh cell in OpenFOAM.

2.2. Interface reconstruction. We have chosen a first order accurate reconstruction algorithm similar to the one of Parker and Youngs (1992) in which the gradient of the volume fraction field determines the orientation of the interface plane with a difference in the accurate and parallelized method of gradient calculation on arbitrary unstructured meshes. This algorithm is first order convergent regarding the geometrical reconstruction error, i.e. it cannot reconstruct planar interfaces exactly. The absolute accuracy in determining the interface orientation comes from the connectivity provided by the cell stencil on which the volume fraction gradient is computed. accurate gradient calculation method on a structured mesh is the Mixed Youngs-Centered (MYC) gradient calculation method, developed by Aulisa et al. (2007). Using a wider stencil to increase the accuracy in computing the interface normal introduces numerical smoothing of the interface curvature, as reported by Kothe et al. (1996). This is a common issue of the geometrical VoF algorithm, however, since the reconstruction error reduces with the increase of mesh density, the application of local dynamic AMR significantly reduces both the reconstruction errors and the need for a reconstruction algorithm of higher order. Additionally, the overall computational overhead of the solution algorithm is significantly reduced by reducing the number of cells compared to a static uniformly refined mesh.

The overall reconstruction algorithm is described by Algorithm 1, defined by two key steps: gradient calculation and interface positioning.

Algorithm 1 Reconstruction algorithm

```

compute the gradient of the volume fraction
for cells do
  if cell is an interface cell then
    initialize the iterative positioning
    while interface not positioned do
      secant method: update position
      if secant diverging (two arguments outside search interval) then
        while interface not positioned do
          bisection method: update position
        end while
      end if
      update secant divergence test (store last argument)
    end while
  end if
end for

```

2.2.1. *Gradient calculation.* Calculating the volume fraction gradient to second order of convergence on an unstructured mesh has been investigated mostly for single phase simulations (e.g. Mavriplis (2003)) and for volume rendering algorithms in the field of Computer Graphics (e.g. Correa et al. (2011)). When it comes to two-phase flows on unstructured mesh, an overview of the possible gradient schemes is provided by Kothe et al. (1996). Ahn and Shashkov (2007) have used a least squares approach for gradient calculation on an unstructured mesh for comparing the results with their MoF reconstruction.

A steep change of the volume fraction field across the fluid interface within a single cell layer introduces difficulties in obtaining an accurate gradient calculation on unstructured meshes. Computation of the gradient on unstructured meshes based on the approximation stemming from the Gauss divergence theorem is of second order convergence, however, this gradient scheme does not take into account point cell neighbors. Therefore, the absolute accuracy of such schemes deteriorates on fields with large jumps in values, across a narrow band of cells. In the case of our geometrical VoF algorithm, the reduced absolute accuracy of the standard Gauss gradient is observed in the form of instabilities of the reconstructed interface geometry. The instabilities persist regardless of the choice of the interpolation scheme, since the interpolation stencil remains unchanged. This is especially true for tetrahedral and hexahedral unstructured meshes. On polyhedral meshes, each cell is connected to all neighbor cells by sharing a common face. The face-based gradient calculation on polyhedral meshes is thus more accurate.

We have used a *Node Averaged Gauss* (NAG) gradient scheme to compute the orientation of the interface normal. The NAG gradient relies on the connectivity which is already provided by the unstructured mesh. However, the increase in absolute accuracy comes from successive interpolation of cell centered values to mesh points, and averaging of the point values at face centers. The value of the field is interpolated from cell centers to cell points using an Inverse Distance Weighting (IDW) interpolation:

$$(2.6) \quad \phi_p = \sum_{pc} w_{pc} \phi_{pc}$$

where pc marks cells c surrounding the mesh point p (point-cells), ϕ_p is the field value which maps to mesh points, and w_{pc} is the inverse distance weight:

$$(2.7) \quad w_{pc} = \frac{1}{\sum_{\tilde{pc}} \frac{1}{\|\mathbf{x}_p - \mathbf{x}_{pc}\|}},$$

between the center of the point-cell pc and the mesh point p .

From the mesh point values, the face-centered values are calculated using *area weighted averaging*. As a first step, the center of the face is calculated as the algebraic average of the face points, and the initial face-centered value ϕ'_f is computed by algebraically averaging the point values:

$$(2.8) \quad \phi'_f = \frac{1}{N_{fp}} \sum_{fp} \phi_{fp},$$

where ϕ_f is the *initial face centered value*, fp is a set of mesh points that comprise a face f (face-points) and N_{fp} is the number of face-points. In a second step, the face is decomposed into triangles using the face center and points of each face edge (fp , $fp+1$). Triangle area is computed using the vector product its edge

vectors, and is then used as a weighting factor: the final face centered value is then computed as an area weighted average of the averaged triangle values:

$$(2.9) \quad \phi_f = \sum_t w_t \phi_t,$$

where w_t is the area weight of the triangle:

$$(2.10) \quad w_t = \frac{A_t}{\sum_t A_t},$$

and ϕ_t is the average value of the triangle:

$$(2.11) \quad \phi_t = \frac{1}{3}(\phi'_f + \phi_{fp} + \phi_{fp+1}).$$

As a final step in computing the cell centered gradient, the face centered field is used to calculate the gradient using the Gauss divergence theorem in the gradient form:

$$(2.12) \quad \nabla \phi_c \approx \frac{1}{V_c} \sum_f \phi_f \mathbf{S}_f.$$

This algorithm accounts for the volume fraction values stored in *skew cells* (cells which are connected with the cell in question through a point or an edge) with their information to be transferred to the interface cell indirectly, without the explicit computation of the additional connectivity required by the wide cell stencil on the unstructured mesh.

The area weighted averaging takes into account the contribution to the final face-centered value by taking into account the shape of the face. An alternative calculation of the NAG gradient could involve IDW interpolation applied to compute the face centered values instead of the area averaging procedure. This alternative has not been tested since the above averaging approach has been used to produce very accurate as well as convergent interface reconstruction results.

The *generalized least squares gradient* (generalized LSQ) that supports arbitrary unstructured meshes as described by Mavriplis (2003) has also been implemented. For the generalized LSQ gradient, the connectivity stencil storing the access information to cell point neighbors needs to be constructed. For a linear least squares gradient, the field is approximated using the linear part of the Taylor series, i.e.

$$(2.13) \quad \phi(\mathbf{x}_k) \approx \phi(\mathbf{x}_c) + \nabla \phi(\mathbf{x}_c)(\mathbf{x}_k - \mathbf{x}_c),$$

where c and k are the indirect access indices of two cell centers on an unstructured mesh. Since a wider cell stencil on a three-dimensional mesh implies a larger number of cell centers than three, a gradient of a scalar field ϕ_c is computed by minimizing the weighted gradient error for each cell c :

$$(2.14) \quad E_c = \sum_k w_{ck}^2 E_{ck}^2,$$

where the error is defined as ((Mavriplis, 2003))

$$(2.15) \quad E_{ck} = -[\phi(\mathbf{x}_c) - \phi(\mathbf{x}_k)] + \nabla \phi(\mathbf{x}_c)(\mathbf{x}_c - \mathbf{x}_k),$$

and the w_{ck} is the inversed distance weight. The minimization of the error E_c for a scalar field results with a solution of a algebraic equation system for each cell of dimensions 3×3 , with the dimensions defined by the three components of the gradient vector.

2.2.2. Interface positioning. An iterative approach to interface positioning (Rider and Kothe (1998)) using the super-linear convergent Brent's algorithm (Brent (1971)) or an analytical approach (Scardovelli and Zaleski (2000)) can be chosen for interface positioning. Ahn and Shashkov (2007) have shown that the interface positioning may be accomplished in a simpler way, using a combination of the secant and bisection iteration methods. The bisection method has guaranteed linear convergence, and the secant method has super-linear convergence, but may diverge.

Figure 3 shows the details of our interface positioning algorithm. A characteristic fill level function is shown which corresponds to the increase of the volume fraction value as the interface is moved along the orientation axis given by the gradient of the volume fraction. Because of the monotonicity of the fill level function we know that the fill level function has a zero value within the search interval. However, divergence of the secant method may happen when the iterative procedure reaches the border of the interval since the fill level function has a *vanishing slope* at the interval borders ($-\alpha$ or $1 - \alpha$), so the iterative procedure switches to the bisection method in this case.

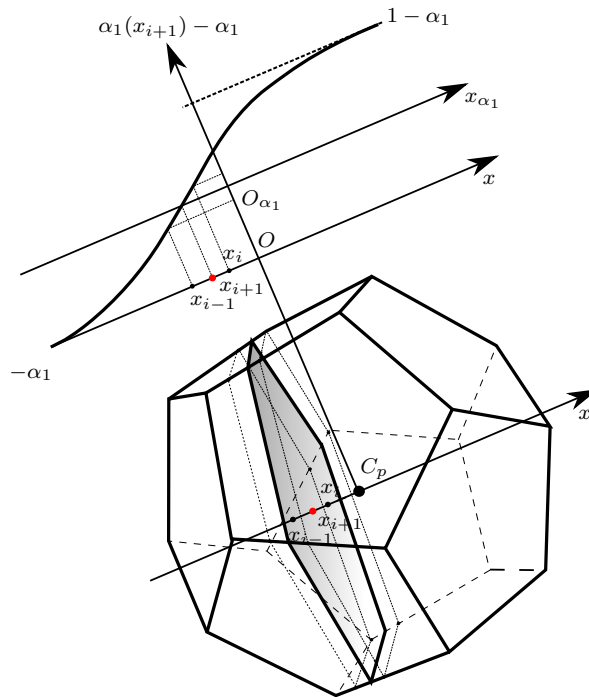


Figure 3. Geometric Reconstruction: Interface positioning.

2.3. Volume fraction advection. Advection of the volume fraction is based on a geometrical computation of the *fluxed phase volume* V_α on cell faces. This is achieved by *sweeping* (backtracking) the face along the streamline vectors given by the interpolated velocity field at the mesh points:

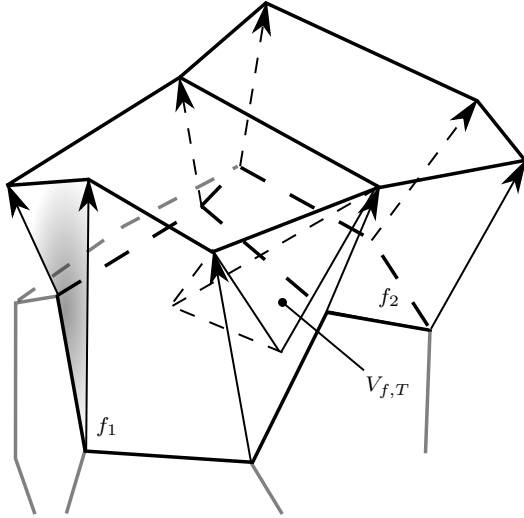
$$(2.16) \quad \mathbf{x}'_{fp} = \mathbf{x}_{fp} - \mathbf{U}_{fp} \Delta t,$$

where \mathbf{x}_{fp} is the face-point (a mesh point addressed via the cell face index list). The swept face, together with the original face, construct together a so-called *congruent* polyhedron, which may have non-planar faces and may even be non-convex. The advantage of using unique point velocities lies in the fact that the *swept polyhedra do not overlap at all*, as shown in Figure 4a. However, it has been reported in the literature (Liović et al., 2006) that using the full discrete flow map may result in highly distorted polyhedra when complex flow fields are present, introducing errors in mass conservation and numerical boundedness of the volume fraction field. To the contrary, as we show later in the results part, below the expected Courant number limit ($Co < 1$) our development of the numerical flow solution remains mass conservative and bounded within $[0, 1]$ using point velocities, even for complex flow fields and both on meshes with densities used for standard test cases and on dynamically refined meshes using local dynamic AMR. We have observed an increased accuracy and robustness of the advection algorithm because of the tetrahedral decomposition applied to the computation of the volume of the swept polyhedron. Analytical expressions for computing the volume of the flux polyhedron rely exclusively on the convexity of the polyhedron. Using unique point velocities to sweep the face does introduce some non-planarity of the faces of the swept as shown for an example shaded non-planar face in Figure 4a. However, the distortion of the polyhedron will always be small enough, such that the tetrahedral decomposition removes the face non-planarity and delivers accurate results for the volume of the swept polyhedron S_f with non-planar faces, which allows for an efficient iterative flux correction procedure that completely avoids topological operations on the swept polyhedron.

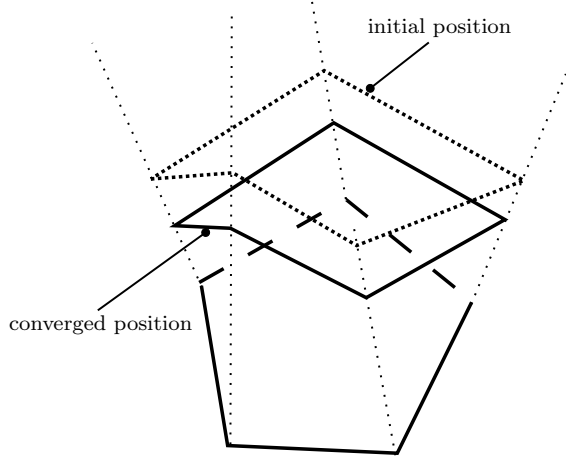
Figure 4a shows the construction of the swept polyhedron: face point velocities \mathbf{U}_{fp} are interpolated using (2.6) and multiplied by $-\Delta t$ to track the face back (Equation 2.16). Tetrahedral decomposition is then used to compute the volume of the volumetric flux per each face f and the polyhedron face is swept along the stream vectors iteratively (Figure 4b) until the volume of the swept polyhedron becomes equal to the volume given by the volumetric flux F_f :

$$(2.17) \quad V_{f,F} = \|F_f\| \Delta t,$$

converging into the final *flux polyhedron* used to compute the volume of the fluxed phase across face f . The velocity field obtained at the face points using inversed distance interpolation is not divergence free in the discrete sense, thus a divergence correction becomes necessary. For this, we define the volume of the



(a) Sweeping faces with point velocities produces non-overlapping swept polyhedra.



(b) Iterative correction of the swept polyhedron to match the volume given by the volumetric flux.

face-swept flux polyhedron:

$$(2.18) \quad V_{f,S} = \sum_{f,T} V_{f,T},$$

where $V_{f,T}$ is the volume of a tetrahedron produced as a result of tetrahedral decomposition of the swept-face polyhedron S_f generated for each face f of the mesh (Figure 4a). Using the volume of the decomposed face-swept flux polyhedron, the discrete swept volumetric flux can be computed as

$$(2.19) \quad F_{f,S} = \frac{V_{f,S}}{\Delta t}.$$

As already noted, this volumetric flux is not expected to satisfy the discrete divergence free condition (2.4) necessary for the mass (volume) conservation of a pseudo-staggered solution algorithm, i.e.

$$(2.20) \quad \sum_f F_{f,S} \operatorname{sgn}(F_f) \neq 0,$$

where $\operatorname{sgn}(F_f)$ is the sign function of the volumetric flux:

$$(2.21) \quad \operatorname{sgn}(F_f) = \begin{cases} +1, & F_f > 0 \\ -1, & F_f < 0. \end{cases},$$

which needs to be computed once per face since the volume of the swept-face polyhedron will always be positive. Subsequently a *divergence correction* of the swept polyhedrons is to be performed to ensure mass conservation. This practice has proven sufficient for the computation of the fluxed phase volumes, since the point velocity field is then only needed to provide the direction for face sweeping (streamline direction).

In literature, there are three approaches commonly used for the divergence correction: a scalar coefficient correction (Liović et al., 2006), analytical correction (Hernández et al., 2008) and a parametric correction (Mencinger and Žun, 2011). We have developed a novel efficient and iterative approach: the *swept polyhedron* computed by sweeping the face is corrected iteratively until its volume is equal to the volume given by the fluxed volume defined by the scalar volumetric flux (Equation 2.17). The super-linear convergent secant method is applied to *move the end points of the flux polyhedron* until its volume corresponds to the volumetric flux volume. This algorithm does not involve topological changes of the flux polyhedron and the method converges in a very small number of steps (3-5 on average, evaluated for the shear flow test case) to machine tolerance since the initial volume of the flux polyhedron is in magnitude near to the magnitude of the volumetric flux, and the target function is a fill level function with a monotonic increase. Avoiding topological operations in the correction of the flux polyhedron increases the speed of the correction significantly. We have tested the algorithm for different shapes of swept faces, applying random perturbations in the orientation of swept edges and have found the correction algorithm to be robust and accurate. Even with random perturbations of swept point coordinates in magnitudes up to 20% of the characteristic length of the face (Figure 4a), the calculation of the volume magnitude remains correct to machine tolerance, allowing for the iterative correction algorithm to converge very quickly.

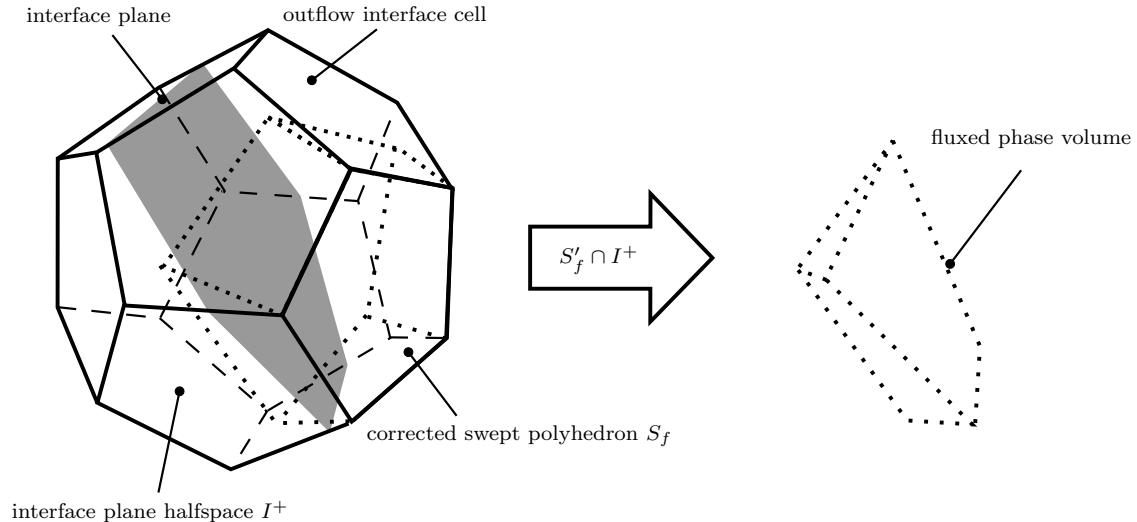


Figure 4. Computing the volume of the fluxed phase using intersections..

After the swept polyhedrons have been corrected, the contributions of the volumetric phase flux coming from the surrounding cells needs to be computed. Obtaining a flux contribution using geometrical intersections is shown schematically in Figure 4 for a single face. The corrected swept polyhedron S_f (dotted lines) is initially clipped with each cell of the advection stencil:

$$(2.22) \quad S'_f = S_f \cap C_s,$$

where C_s is the cell of the chosen flux stencil s . The flux stencil s needs to incorporate point and edge face neighbors, otherwise those contributions to the total fluxed phase volume will be missing and interface motion will be artificially distorted in those directions, as is the case for flux-based methods naively utilizing algebraic advection schemes on unstructured hexahedral meshes. In case the candidate cell is an interface cell, a subsequent intersection is performed with the positive halfspace I^+ defined by the PLIC plane (grey colored polygon):

$$(2.23) \quad S''_f = S'_f \cap I^+.$$

This is the final face contribution to the total fluxed phase volume as illustrated in Figure 4. The total value of the volumetric flux is then computed as the sum of the fluxed phase volume contributions calculated for all cells of the face flux stencil. The calculation of the total fluxed phase volume across a face is performed for an *outflow cell* only using (2.3), resulting in a final decrease of the volume fraction for this cell, and the corresponding increase for the *inflow cell*.

We use a *narrow band* of interface cells for the advection of the volume fraction field. Since geometrical intersections are needed for the geometrical reconstruction and advection steps, localizing the computation to a narrow band of cells strongly increases the efficiency of the overall algorithm. In case of a complex velocity field and a naive advection operating on the whole domain, *wisps* appear in the bulk of both phases. Hence, locating and removing wisps is greatly simplified for a *narrow band* advection since their initial location is always in the bulk cells that are direct neighbors to interface cells. To remove the wisps, a redistribution algorithm of Harvie and Fletcher (2000) has been implemented, with applied modifications that are necessary for fast computation of large stencils on arbitrary unstructured meshes. Both void and phase wisps are redistributed conservatively to the surrounding interface cells, under the constraint that the removal of mass or its addition is not allowed to cause further creation of over/undershoots or wisps.

The narrow cell band is constructed using neighborhood cell information and the volume fraction field, i.e. the algorithmic task for the advection is: advect only in interface cells and their first *point neighbors*. To avoid computing additional point-cell neighbor connectivity which would then be updated during the evolution of the interface, we have re-used the gradient of the volume fraction field as an indicator for the bulk cells that are not involved in the advection. This is schematically shown in Figure 5a. A bulk cell is characterized as a cell for which the gradient of the volume fraction is zero.

Since only the outflow from cells is calculated, the change of the volume fraction is not applied for cells that lie in the bulk of the phases. The fluxed phase volume is computed also for cell faces when the outflow

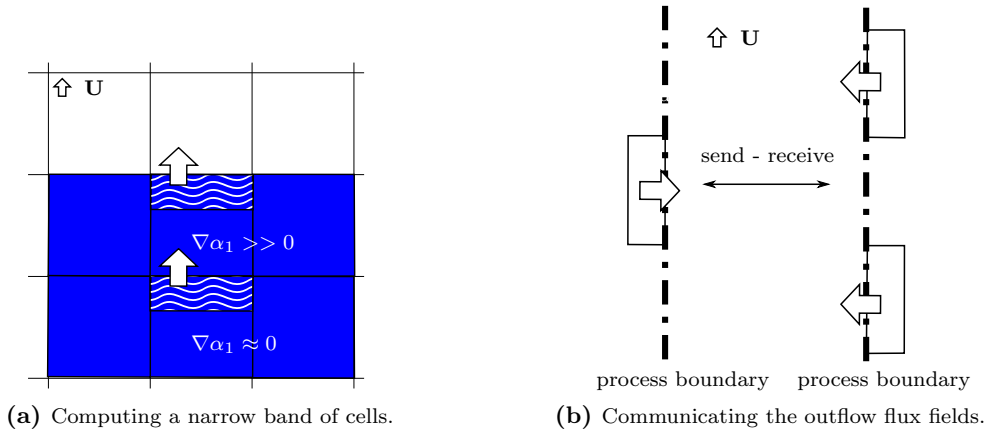


Figure 5. Parallel implementation: computing the fluxed phase volume.

is present for the bulk cell. However, in this case the update of the volume fraction field is not executed for the bulk cell. The re-use of the gradient field as a criterion for constructing the narrow band of cells involved in the advection significantly increases the efficiency of the method, since the gradient is already computed as a requirement of the reconstruction algorithm.

2.4. Parallel implementation. The parallel implementation of the reconstruction algorithm is simplified when the NAG gradient is utilized for the computation of the interface normal, since no additional communication structures need to be prepared and communicated over the process boundary. In the case of the generalized LSQ algorithm, computing the additional connectivity involves multiple issues: parallel communication involving more complex stencil structures, update of the stencil structures when topological changes are applied to the mesh (AMR), and caching of the additional connectivity to increase algorithm efficiency. Since the NAG gradient has provided sufficiently accurate results, we have left the parallel implementation of the generalized LSQ gradient as future work if proved to be necessary.

Using the gradient to determine the bulk cells simplifies the parallel implementation of the advection algorithm as shown schematically on Figure 5a. Additional connectivity required to identify the cell candidates would otherwise be communicated across process boundaries, as well as the geometrical information of the mesh cells. However, when the volume fraction gradient is used to determine the narrow band of cells, there is no need for additional connectivity. Since the outflow field is computed for each separate domain, the boundary outflow fluxes need to be exchanged (simultaneously) across process boundaries. The outflow from one domain represents the inflow field for the other domain, as shown in Figure 5b. In order to avoid *dead-locking* resulting from simultaneous communication, the parallel code utilizes *non blocking* communications (Gabriel et al., 2004).

3. Geometrical mapping of the volume fraction field for local adaptive mesh refinement

Although the geometrical VoF algorithm supports arbitrary cell shapes, the mesh topology dictates the concrete strategy and conceptual approach (i.e. type of topological operations) for mesh refinement. We are applying local dynamic AMR to increase the solution accuracy especially in the vicinity of interfaces, in particular for the coupling between the geometrical algorithm and the flow solution. The algorithm for local dynamic AMR in OpenFOAM is developed on the basis of the unstructured *hexahedral* mesh: it is based on a *fully unstructured mesh refinement* procedure. Fully unstructured mesh refinement has the advantage to deal with flow domains of arbitrary geometrical complexity, since the topological operations on the mesh are done directly, changing the overall mesh connectivity information. However, since the connectivity information is changed by the topological operation, the mesh data structures need to be modified in order to store the new connectivity produced by the refinement cycle.

If the topological operation introduces a production of mesh data, the capacity of the data structures needs to be extended. This involves re-allocating memory and extending the capacity of the data structures, which sets a computational price to the flexibility in dealing with arbitrary complex geometries. Even so, the mesh refinement engine in OpenFOAM, together with the mapping of all intensive properties, takes up only a small fraction of the overall time involved in the flow solution.

The refinement cycle consists of two sub-cycles which may be executed, depending on the refinement criteria: refinement and un-refinement sub-cycle. If both sub-cycles are executed, the mesh information from the beginning of the refinement cycle is lost in between the sub-cycle execution. Removal of intermediate information makes it impossible to map the mesh modified by two subsequent refinement cycles to the initial un-refined mesh to which the interface geometry maps. The obstructed mapping renders the refinement

procedure unusable together with the geometrical transport algorithm. For this purpose, we have extended the dynamic mesh capability to store the connectivity information relative to the unmodified mesh state at the beginning of the refinement cycle. This further enables the execution of a *geometrical mapping algorithm* for the volume fraction field described by Algorithm 2.

Algorithm 2 Geometrical mapping algorithm for the volume fraction field

```

initialize the absolute cell map
if cells to be refined exist then
    mark mesh as refined
    refine mesh
    absolute cell map = current cell map
end if
if cells to be unrefined exist then
    mark mesh as unrefined
    copy the absolute cell map
    un-refine mesh
end if
if mesh is refined and unrefined then
    for current cell map do
        absolute cell map [cell] = absolute cell map[current cell map[cell]]
    end for
else if mesh is unrefined then
    absolute cell map = current cell map
end if
for absolute cell map do
    intersection = intersect (interface planes [absolute cell map [cell]], cell)
    volume fraction [cell] = intersection / cell volume
end for

```

The interested reader is directed to our forthcoming publication of the authors for details regarding the description of the unstructured mesh topology in OpenFOAM and its reflection onto the geometrical mapping algorithm for the volume fraction field (Marić, Marschall, and Bothe, 2013).

4. Results

4.1. Verification of the interface reconstruction. For structured meshes, a standard approach to computing the error of the interface reconstruction algorithm (i.e. reconstruction error) resorts to computing the volume that lies between the piecewise planar reconstructed interface geometry and an analytical function representing the true interface (e.g. the surface of a sphere). This *integration approach* requires sub-integration for each cell. Hence, it is not straightforward to modify the algorithm in order to support arbitrary cell shapes.

On arbitrary unstructured meshes, in order to achieve a single layer of interface cells for a pre-processed volume fraction field, we have adopted the approach by Ahn and Shashkov (2009) that involves intersecting two unstructured meshes: the *base mesh* and the *tool mesh*. The *base mesh* is the mesh used to discretise the flow domain, and the *tool mesh* is used as a tool for cutting the *base mesh* in order to set the volume fraction field. This preprocessing approach of intersecting meshes allows for preprocessing of arbitrarily complex volume fraction fields. Since the tool mesh is unstructured, it may be used to discretize the complex input geometry. Moreover, local refinement can easily be applied near boundaries that are used to describe the fluid interface: this significantly reduces the computational time of the preprocessing. The quality of the tool mesh is of virtually no importance, since it is only used to set the initial volume fraction fields.

In order to compute the reconstruction error on meshes with arbitrary cell shapes, the reconstruction error is defined in each cell as the *volume of symmetric difference* (E_{vsd}) between the reconstructed geometry (*interface polyhedron*) and the true geometry. The true interface geometry is represented by a subset of cells of a tool mesh, i.e. a set of tool mesh boundary faces represent the true discrete interface geometry.

The computation of the reconstruction error for a true interface geometry defined by the tool mesh is performed cell-wise. Error calculation is schematically described in two dimensions in Figure 6. Each mixed cell of the base mesh (dashed line) is intersected with a set of polyhedrons of the tool mesh (green line). Each tool mesh polyhedron is then clipped by the base mesh cell (black line). The reconstruction error (red color) is separated into two contributions: *positive half-space error* (E_{vsd}^+) and *negative half-space error* (E_{vsd}^-), based on the location of the error geometry with respect to the interface plane.

The set of tool mesh polyhedra is separated into two subsets based on the interface plane orientation. The negative half-space error is the volume of symmetric difference that lies in the negative closed half-space

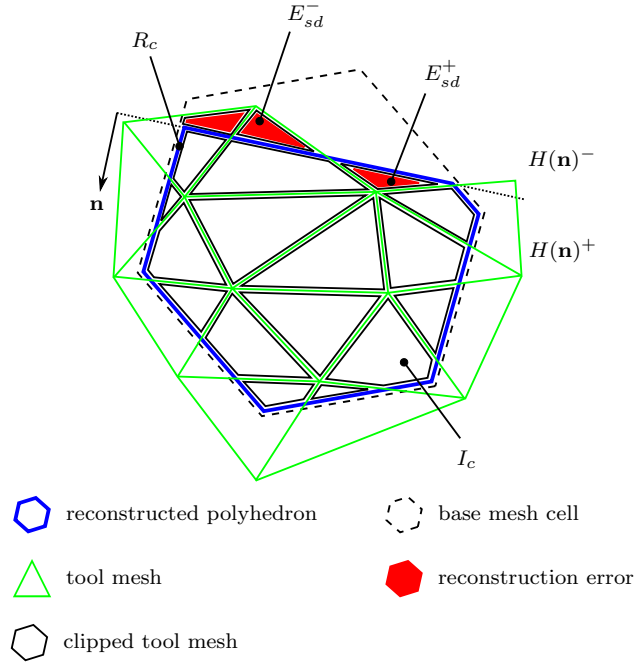


Figure 6. Volume of symmetric difference reconstruction error.

defined by the interface plane. It is computed as an intersection between the set of the tool mesh polyhedra clipped by the cell (I_c) and the negative half-space ($H(\mathbf{n})^-$), defined by the interface plane:

$$(4.1) \quad E_{vsd}^- = ||H(\mathbf{n})^- \cap I_c||.$$

The positive half-space error is calculated as the algebraic difference between the volume of the reconstructed (PLIC) polyhedron (R_c , blue line) and the sum of the volumes of the clipped tool mesh polyhedra (black line):

$$(4.2) \quad E_{vsd}^+ = ||R_c|| - ||H(\mathbf{n})^+ \cap I_c||.$$

The total reconstruction error is computed as the sum of the positive half-space error and the negative half-space error:

$$(4.3) \quad E_{vsd} = E_{vsd}^- + E_{vsd}^+.$$

Note that when the *integration approach* is used to determine the reconstruction error the size of the sub-grid integration intervals will determine the accuracy of the computed error (Aulisa et al. (2007)). The *mesh intersection approach* requires that the mesh density of the tool mesh to be high enough in order to accurately describe the true interface geometry. This is both visually observed and quantified for all validation cases.

4.1.1. *Reconstruction of a sphere.* In this section the reconstruction results for a spherical interface on an unstructured hexahedral, tetrahedral and polyhedral mesh are presented.

Figures 7 and 8 show the convergence diagrams of the volume of symmetric difference reconstruction error on a box domain of dimensions $[0, 1]^3$ which is discretized with an *unstructured hexahedral mesh*. Although the discretization results in cuboid finite volumes, the mesh connectivity is still unstructured. The first order Youngs algorithm exhibits the behavior as described by Ahn and Shashkov (2007): on coarse meshes the order of convergence of the error is higher and as the base mesh density increases, the order reduces to around one. For the fine tool mesh, the order of convergence as described by Aulisa et al. (2007) is 2.22 for the coarsest base mesh and 1.37 for the finest base mesh.

Different mesh densities were tested for a spherical tool mesh. The local refinement of the tool mesh near the interface makes the total number of cells not important rather the number of faces used to approximate the spherical surface is central. Figure 9 shows two *tool meshes* of a sphere, each with the same number of face elements, but different number of volumes. Both meshes are cut such that the inner mesh is visible: the refined mesh has much less volumes, and both meshes describe the spherical surface with the same mesh density. The tool mesh does not need to be of high quality since it is not a part of the solution process, i.e. it is used only for the preprocessing of the volume fraction field. Figure 10 shows the convergence for the

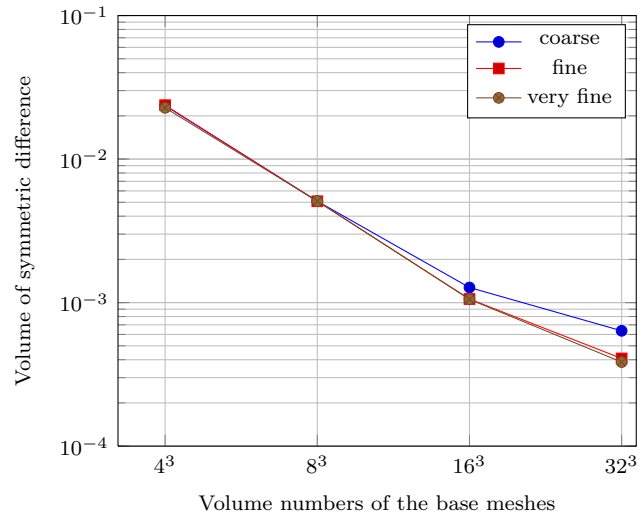


Figure 7. Reconstruction error for a sphere using the NAG gradient, on an unstructured hexahedral mesh.

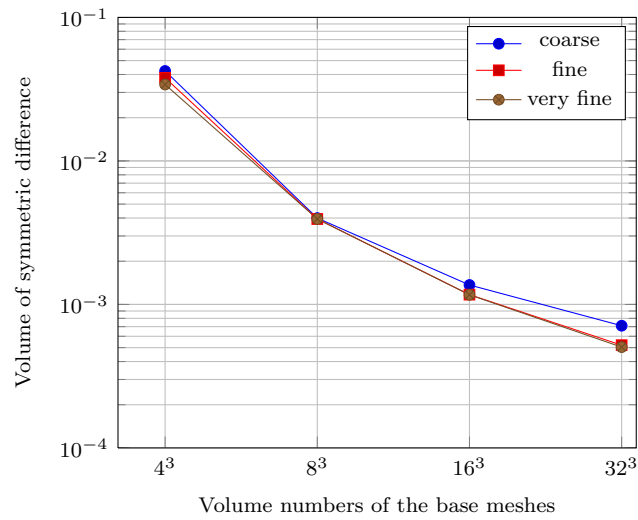


Figure 8. Reconstruction error for a sphere using the generalized LSQ gradient, on an unstructured hexahedral mesh.

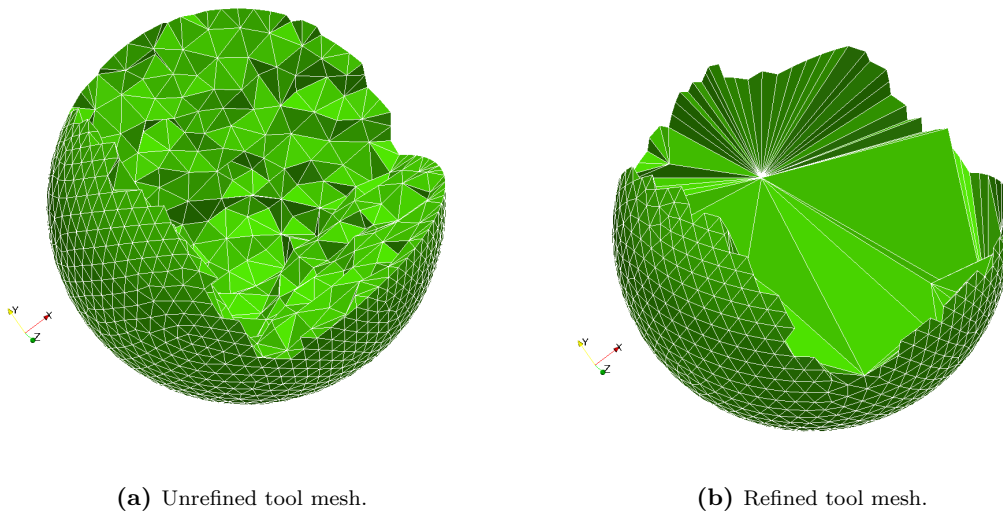


Figure 9. Tool meshes of a spherical interface.

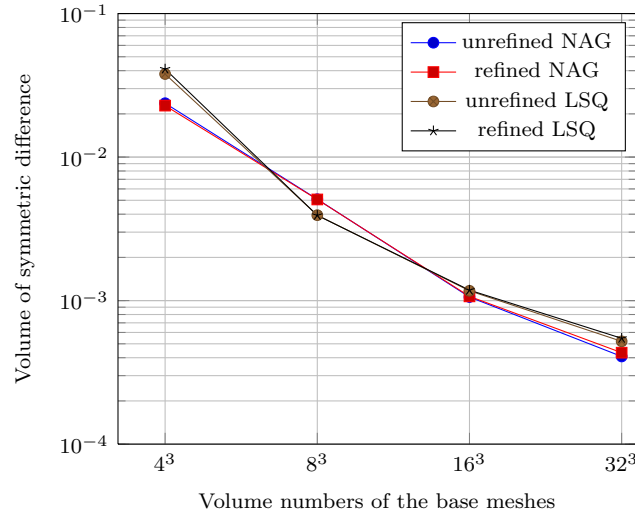


Figure 10. Comparison of the reconstruction error convergence for the refined and unrefined tool mesh for a sphere.

reconstructed spherical interface on an unstructured hexahedral mesh with two sphere tool meshes, namely a refined sphere, and an unrefined sphere (cp. Figure 9).

For the mesh convergence study we have used spheres discretized with 956, 3786 and 16462 faces⁴. The surface mesh densities of the sphere correspond to the case labels *coarse*, *fine* and *very fine* used in the Figures 7 and 8. The *fine* sphere mesh is chosen for further results comparison.

Figure 11 shows the input mesh for the sphere (*fine* case) and the comparison of the corresponding reconstructed interfaces using both the NAG gradient and the generalized LSQ gradient on unstructured hexahedral meshes. The NAG gradient shows better results on the coarsest hexahedral mesh in the volume of symmetric difference error. This can be seen when the absolute values are compared for the coarsest *base meshes* shown in Figures 7 and 8. Also, the visual appearance of the interface geometry on the coarsest mesh is clearly better when the NAG gradient is applied on an unstructured hexahedral mesh, as shown in Figure 11.

Figure 12 shows the reconstructed spherical interfaces on a tetrahedral mesh. For this case the error magnitude is lower when the NAG gradient is applied. Interface polygons on a tetrahedral mesh are significantly disconnected, especially around the reconstruction points where multiple tetrahedra meet in a mesh vertex. Around those points the volume fraction values will be either very small ($\alpha_1 \approx 0$) or very large ($\alpha_1 \approx 1$) in which cases even the smallest perturbation in the orientation of the interface normal causes significant disconnection of the interface polygons.

Figure 13 shows the behavior of the interface reconstruction error on an *unstructured tetrahedral mesh*. The evaluation of the reconstruction error is done for both the NAG gradient and the generalized LSQ gradient. Both gradients show similar behavior of the error magnitude with respect to the increase of the mesh density. On a tetrahedral mesh the evaluation of the error convergence is not possible, because of its irregular nature. Still, the diagram shown in Figure 13 shows that the magnitude of the reconstruction error does not decrease as fast as on the unstructured hexahedral mesh. This fact brings us to conclusion that the unstructured hexahedral mesh makes a better choice for domain discretization for our geometrical VoF method.

A polyhedral mesh provides direct connectivity via finite volume faces to all surrounding cells which makes the gradient calculation more exact and straightforward since it relies on the connectivity which is already present and involves all available cell neighbors. However, the quality of the polyhedral mesh will rely on the way it is created, which is usually done by agglomerating tetrahedral cells. When tetrahedral cells are agglomerated to create polyhedra, severely non-convex cells with significant non-planarity of faces, appear in the mesh if the original tetrahedral mesh is not produced with the Delaunay algorithm. Severely non-convex cells introduce numerical errors and are unusable together with the intersection algorithms used for the geometrical VoF method.

To the best of our knowledge, a dynamic mesh refinement algorithm based exclusively on polyhedral cells does not exist. Since we are interested in a more accurate spatial resolution in the surrounding of a *moving fluid interface* (achieved by employing local dynamic AMR), the polyhedral mesh results are

⁴The meshes were created with the *open source* application *SalomeCAD*. They can be easily re-created using the multiplication of the default parameters for the maximal edge length provided by the NETGEN-1D-2D-3D algorithm by factors: 2, 4 and 8.

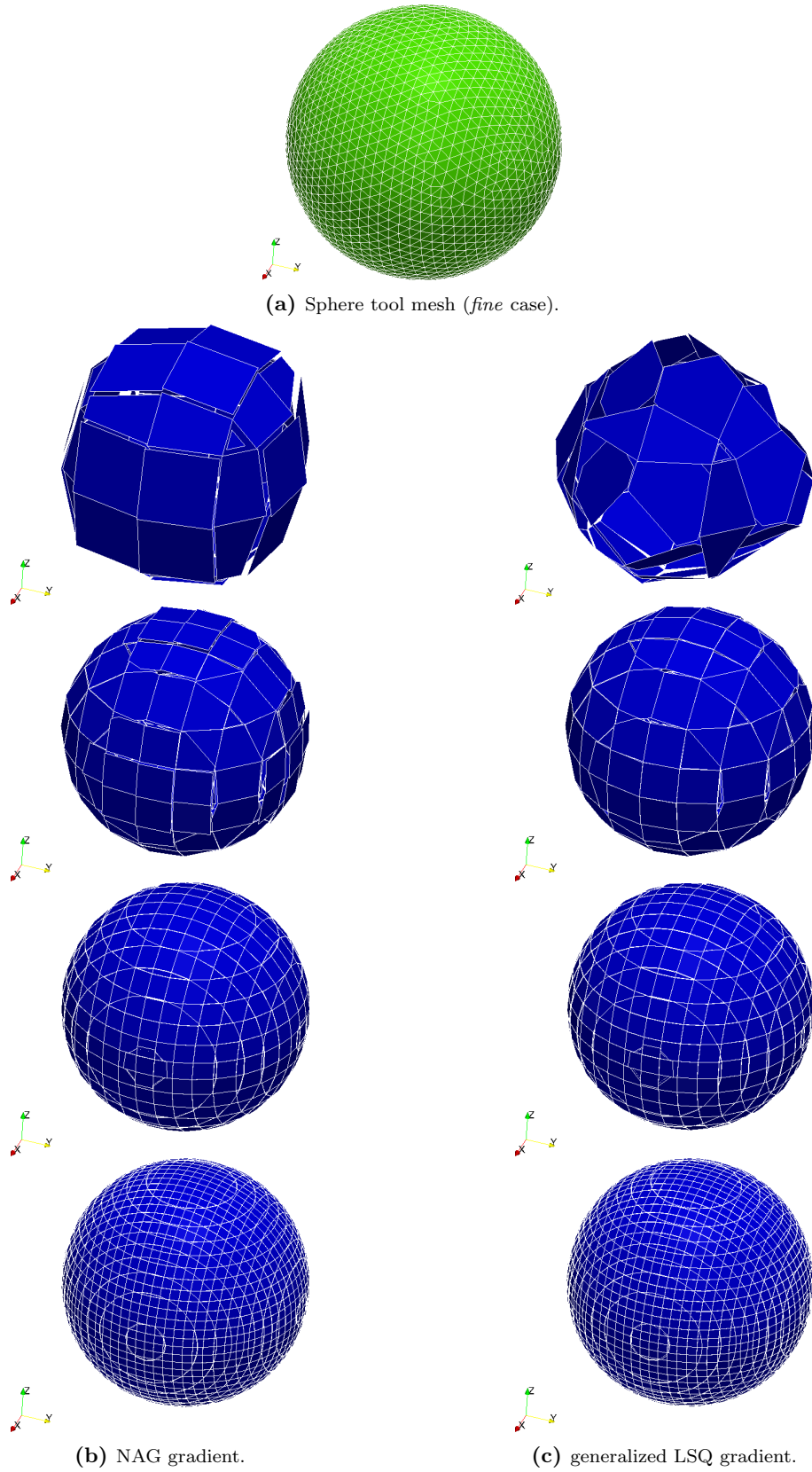


Figure 11. Reconstructed spherical interface on an unstructured hexahedral mesh. Interfaces are reconstructed on base meshes with densities: 4^3 , 8^3 , 16^3 and 32^3 .

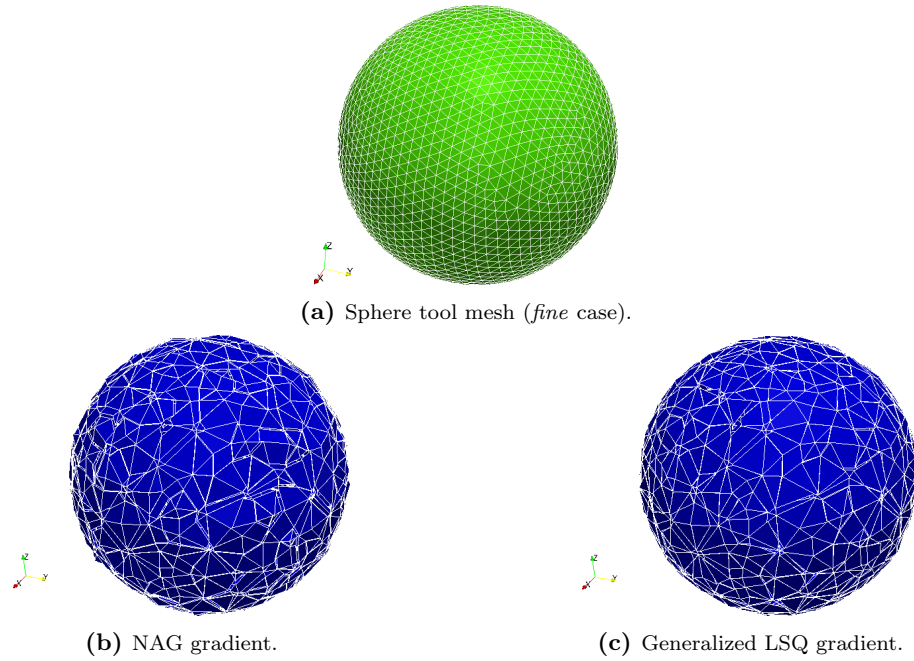


Figure 12. Reconstructed spherical interface on an unstructured tetrahedral mesh. Interfaces are reconstructed on a base mesh with 8774 volumes.

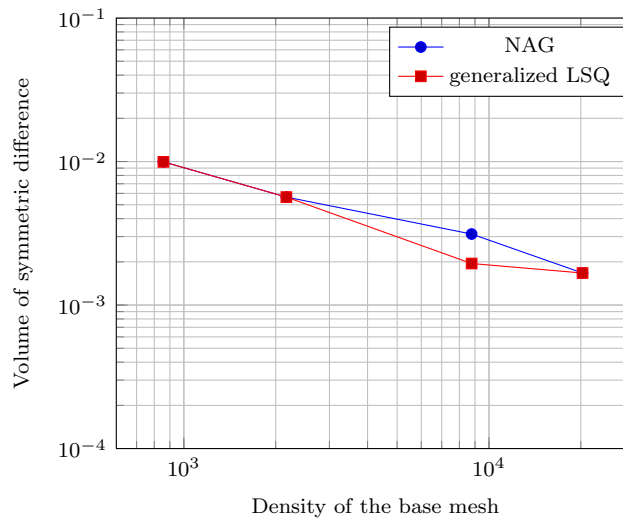


Figure 13. Reconstruction error for a sphere on a tetrahedral mesh with following numbers of volumes: 857, 2168, 8774, 20263.

shown only to prove the generality of the implemented geometrical operations with respect to different cell shapes. 14 shows the reconstruction of a spherical interface on a polyhedral base mesh which is created by agglomerating the tetrahedra of a mesh discretized using equal sized hexahedral cells. The hexahedral cells are then decomposed, each into 24 tetrahedrons, which are then agglomerated into polyhedra to ensure the convexity of the cells. This mesh is then a mixture of hexahedral and polyhedral cells which is clearly visible in the reconstructed interfaces.

The behavior of the reconstruction error shows that there is a significant accuracy gain in reconstructing the interface on an unstructured hexahedral mesh, compared to the unstructured tetrahedral mesh. This type of mesh supports local dynamic AMR within the frame of the existing topological mesh operations in OpenFOAM: hexahedral refinement of cells. Moreover, the automatic mesh generation of unstructured hexahedral meshes is widely available (e.g. via the *snappyHexMesh* tool of the OpenFOAM library). Hence, the unstructured hexahedral mesh presents a natural choice for the domain discretization of a geometrical VoF method supporting local dynamic AMR.

4.2. Verification of the volume fraction advection. In this section the results of the geometrical advection algorithm for standard test cases are shown. Standard test cases are used to validate mass/volume

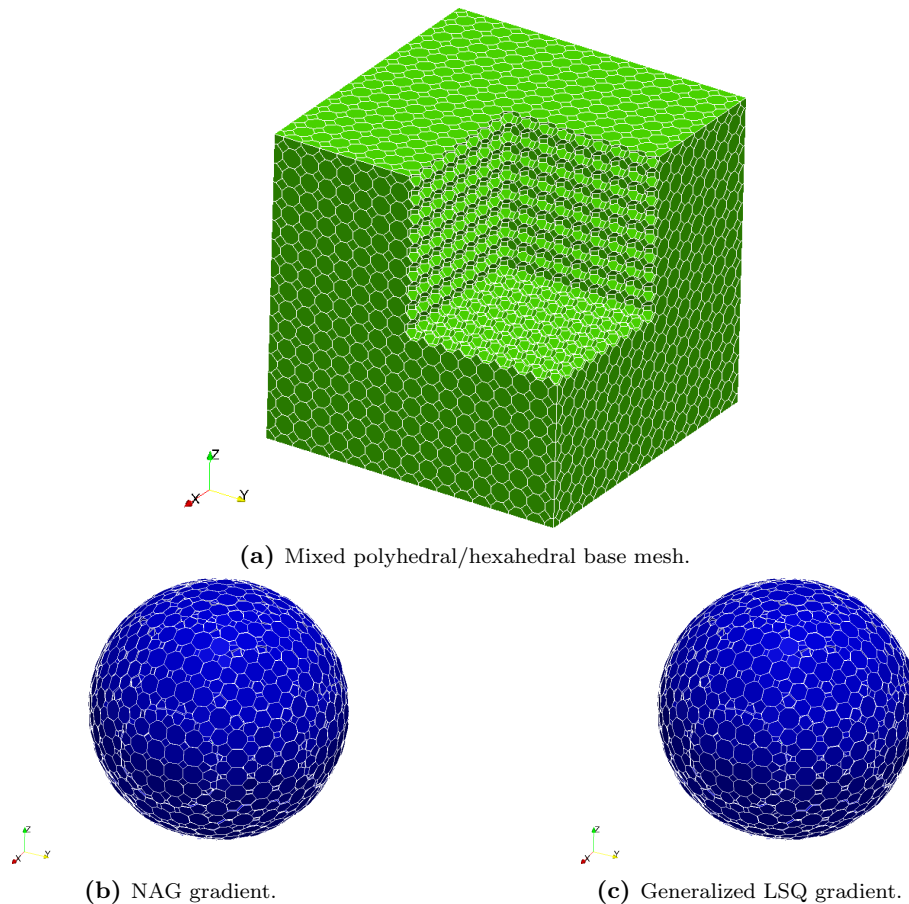


Figure 14. Reconstructed spherical interface on a mixed polyhedral mesh with 22065 cells.

conservation, numerical boundedness of the volume fraction field i.e. $\alpha_1 \in [0 + \epsilon, 1 - \epsilon]$, where ϵ is the reconstruction tolerance, geometrical stability of the interface as well as its *physically consistent motion*. A physically consistent motion of the interface is a motion during which no *artificial separation* is present (e.g. *flotsam/jetsam*), appearance of *wisps* and *artificial deformation* of the interface are reduced to a minimum.

Artificial separation of the interface involves large separated parts of the fluid (flotsam and jetsam), as well as small changes in the volume fraction field (wisps). Flotsam and jetsam are large parts of the interface that separate during the advection artificially, as defined by Noh and Woodward (1976). Wisps are, usually very small, numerically artificial, interface polygons that appear sporadically near the transported interface, as well as within the bulk. In effect, this means that there is an additional layer of cells to the actual interface cell layer, where the values of the volume fraction are either very close to one ($\alpha \approx 1$) or to zero ($\alpha \approx 0$) for cells that are not interface cells. Visualization of bulk wisps, as well as their generation will depend on the reconstruction tolerance of the algorithm. Reducing the reconstruction tolerance, will make the actual bulk wisp cell a full cell, on account of introducing an error in mass conservation for this cell. The presence of wisps in the bulk of the flow is due to the non-divergence-free nature of the discrete flow field, which we counter in our algorithm by introducing a narrow layer of cells where the advection takes place.

Artificial deformation of the interface is an interface motion which, although resulting with a mass conservative volume fraction field bounded between 0 and 1, imposes an artificial change in the velocity with which the interface is locally advected. This error stems directly from the way the volumetric phase flux is computed.

The standard E_g geometrical advection error is defined as follows (Aulisa et al., 2007):

$$(4.4) \quad E_g = \sum_c V_c (\alpha_c(t) - \alpha_c(t_0)),$$

where c marks the cell of the volume V_c , t marks the time value for which the error is computed and t_0 marks the initial (reference) time value. This error can only be applied for advection test cases for which the interface configuration at time t corresponds to the configuration at the initial time t_0 . For such cases, a periodical velocity field is used for advection. Examples of such test cases are described by various authors and we have used the following test cases to verify the geometrical advection algorithm:

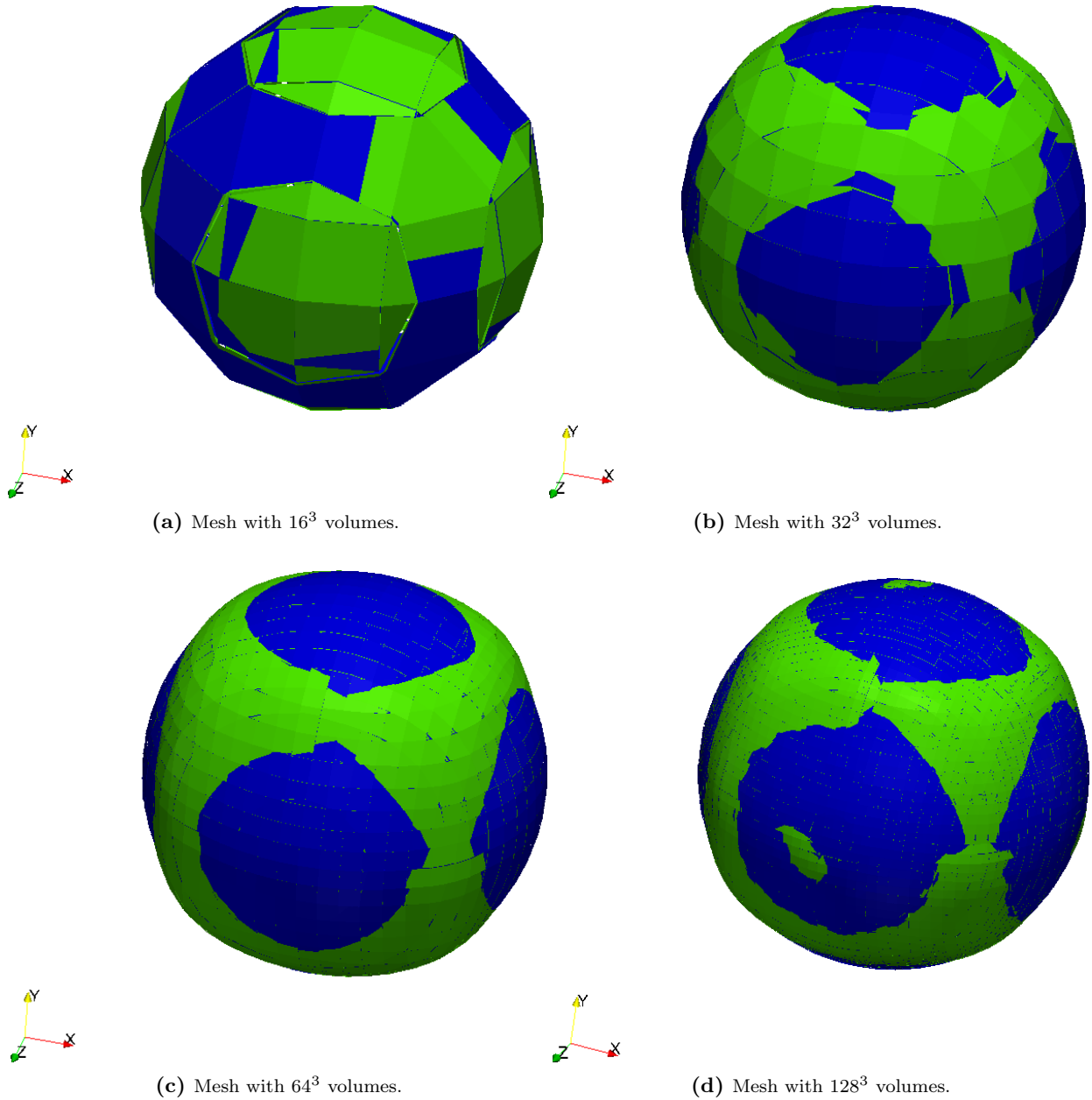


Figure 15. Visual comparison of the initial (blue) and the final sphere shape (green) for mesh different densities of the *skew advection* test.

- periodical translation along spatial diagonal,
- rotation,
- shear,
- deformation.

4.2.1. *Translation and rotation test.* Apart from a sharp interface representation within a single layer of cells, the geometrical VoF method significantly reduces the artificial deformation of the interface compared with algebraic VoF methods. Since there is a contribution to the volumetric phase flux coming from the point-cell neighbor cells (skew cell neighbors), the motion of the interface in this direction will not be artificially changed to a large extent. If the flux contributions stemming from the skew cell neighbors are completely neglected, as this is the case for algebraic advection schemes, interface will be advected adhering to mass conservation, but the interface shape will be artificially changed to a large extent.

The translation test case consists of a sphere of radius 0.15, placed in the center of a unit length box-domain with increasing uniform density, and it is advected with Courant numbers: 0.1, 0.5 and 0.75. The sphere is translated along the spatial diagonal from the initial position to the two corners of the box-domain and returned to initial position at the box center. The overall distance traveled by the sphere in this test case is approximately 10 sphere diameters.

Table 1. Advection errors of the periodical translation test case.

Number of volumes	16 ³	32 ³	64 ³	128 ³
Courant number				
0.1	5.32128e-04	4.24662e-04	8.76037e-04	6.99539e-04
0.5	2.75337e-04	3.85527e-04	7.54332e-04	4.39392e-04
0.75	3.15498e-04	4.10146e-04	6.86752e-04	5.82132e-04

Table 2. Advection errors for the rotation test case.

Number of volumes	16 ³	32 ³	64 ³	128 ³
E_g	8.32758e-04	3.18881e-04	1.45851e-04	1.11573e-04

Table 3. Advection errors for the shear test case.

Number of volumes	16 ³	32 ³	64 ³	128 ³
Courant number				
0.1	1.03638e-02	4.71128e-03	1.49640e-03	5.68667e-04
0.5	1.11825e-02	5.78071e-03	2.59552e-03	1.18850e-03
0.75	1.28960e-02	6.13972e-03	3.27130e-03	1.60405e-03

Figure 15 shows a comparison between the final position of the sphere and the initial sphere position for increasing mesh density and the Courant number of 0.5. For an advection directed along the spatial diagonal, the images show that the flux calculation, although fully un-split, involves a slight deformation of the interface the skew direction. Table 1 shows the geometrical error (E_g) for the skew-translation test case. The relative mass conservation error values are near machine tolerance for the constant translation velocity field and are thus omitted.

The rotation test case consists of a sphere with the radius of 0.15 placed at (0.5, 0.75, 0.5) within a unit-length box domain as described by Jófíre et al. (2010). The sphere is rotated with a Courant number value of 0.5 based on the maximal velocity used to advect the interface. The final and initial positions of the sphere are compared. Table 2 shows the behavior of the advection error E_g with respect to the increase of mesh density for the rotation test case. Figure 16 shows the visual comparison between the final and initial interface shape for different densities of the mesh. The rotation test case involves computing intersections with very thin and distorted flux polyhedra, and for this purpose the rotation test cases with mesh densities of 64³ and 128³ were run in parallel such that the process boundary plane lies orthogonal to the velocity field. This test stresses the robustness and accuracy of the geometrical advection algorithm even for extreme shapes of very thin flux polyhedra.

The visual difference between the initial sphere on the left process boundary (blue) and the final sphere on the right process boundary (green) shown on the Figure 16 is not noticeable. For the coarser meshes of 32³ and 16³ volumes, the overlap shown on a single process domain is insignificant, which is confirmed by absolute values of the E_g error. The error convergence behaves as reported by other authors (Hernández et al., 2008): the error converges faster on coarser meshes and the magnitude of order of convergence magnitude is near 1, since it is defined by the convergence order of the Young’s reconstruction algorithm.

4.2.2. *Shear test case.* The shear test case configuration is described by Liović et al. (2006) in the following way:

$$(4.5) \quad \mathbf{U}(\mathbf{x}, t) = \begin{pmatrix} \sin(2\pi y) \sin(\pi x)^2 \cos\left(\frac{\pi t}{T}\right) \\ -\sin(2\pi x) \sin(\pi y)^2 \cos\left(\frac{\pi t}{T}\right) \\ u_{\max} \left(1 - \frac{r}{R}\right)^2 \left(\frac{\pi t}{T}\right) \end{pmatrix}$$

We have used $T = 3$, $u_{\max} = 1$ and $R = 0.5$ for the case settings to ensure that the shear of the sphere will be extreme, which is visible in Figure 17a. The advection error E_g of the shear test case is shown on the Table 3. The velocity field of the shear flow test case is changing both in time and space, so the Courant number values are computed for the maximal velocity in the flow domain for the current time step. This Courant number value is then used to correct the time step for the next iteration in order to maintain the prescribed fixed maximal Courant number.

Figure 17 shows the extreme state of the sphere in an imposed shear flow, as well as the comparison between the initial and the final sphere state for a mesh of 64³ volumes. The validation test cases with mesh densities of 64³ and 128³ were run in parallel in order to validate the computation of the volumetric phase flux across process domains for complex flows. No differences in the results between the parallel and serial

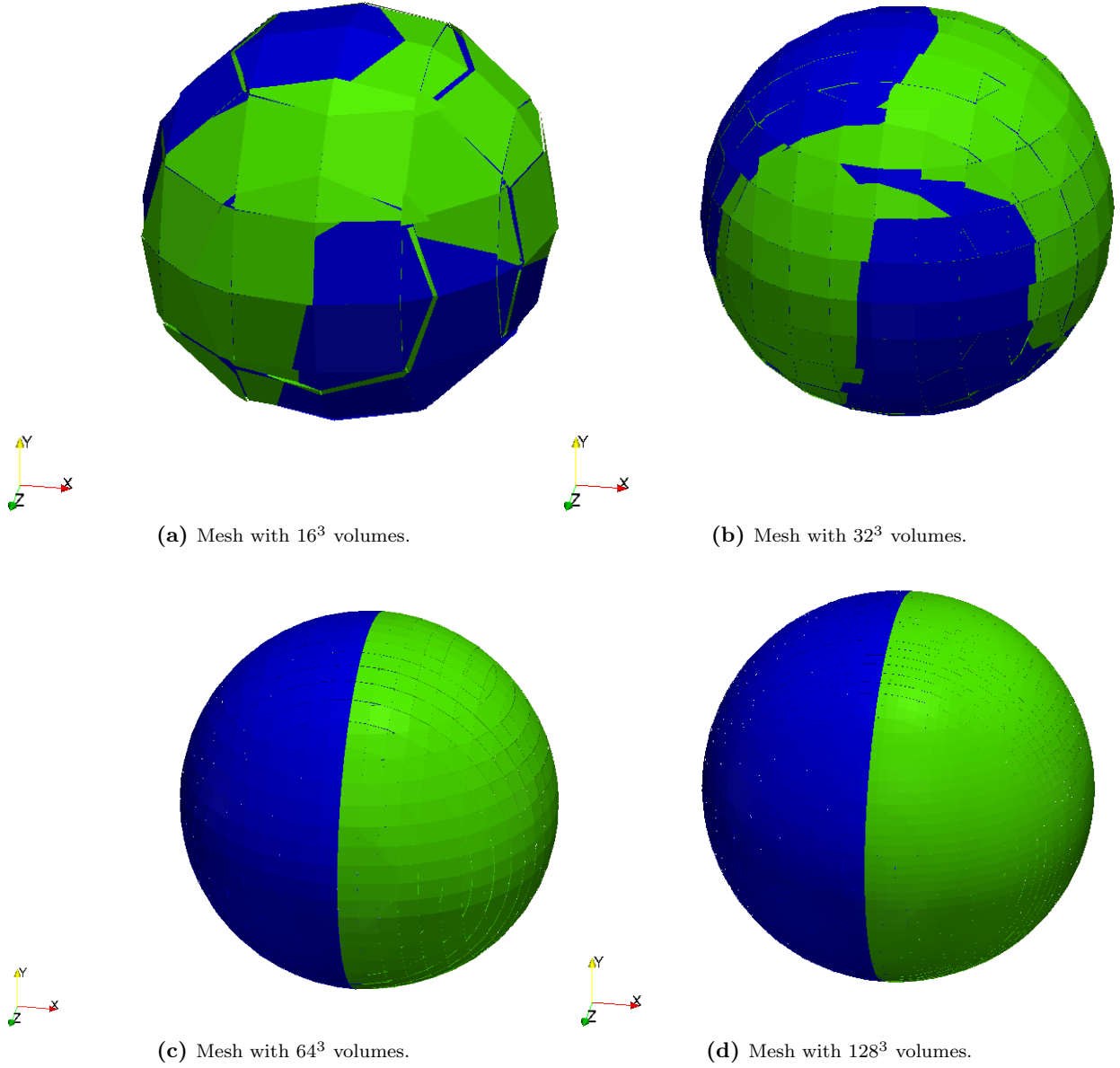


Figure 16. Visual comparison of the initial (blue) and the final (green) sphere shape for different densities of the *rotation* test.

runs have been observed. The static parallel domain decomposition is shown in Figure 17a with different colours.

The quantitative results shown in the Table 3 as well as the results shown in Figure 17 present first (to the best of our knowledge) numerically stable (mass conservative and numerically bounded) results involving a three dimensional spatially complex and time-varying velocity field used to advect the volume fraction with a directionally un-split advection algorithm using a full discrete Lagrangian flow-map on an unstructured mesh hexahedral mesh, in parallel.

4.2.3. *Deformation test case.* The deformation test case, as described by Hernández et al. (2008), reads

$$(4.6) \quad \mathbf{U}(\mathbf{x}, t) = \begin{pmatrix} 2 \sin(2\pi y) \sin(\pi x)^2 \sin(2\pi z) \cos\left(\frac{\pi t}{T}\right) \\ -\sin(2\pi x) \sin(\pi y)^2 \sin(2\pi z) \cos\left(\frac{\pi t}{T}\right) \\ -\sin(2\pi x) \sin(2\pi y) \sin(\pi z)^2 \cos\left(\frac{\pi t}{T}\right) \end{pmatrix}$$

and we chose $T = 3$ to ensure extreme deformation of the sphere. Table 4 shows the advection error values E_g for deformation test cases of different Courant numbers, 0.1, 0.5, and 0.75, as well as increasing mesh densities, 16^3 , 32^3 , 64^3 and 128^3 . Figure 18b shows a comparison between the initial and final interface for the maximal Courant number 0.5 and the mesh density 128^3 , and Figure 18a shows the extreme deformation of the sphere for the same parameter values.

The geometrical instability present in the lower-middle part of the deformed interface in the extreme shear state is visible in Figure 18a. The cause of the instability lies in the fact that the interface in this region

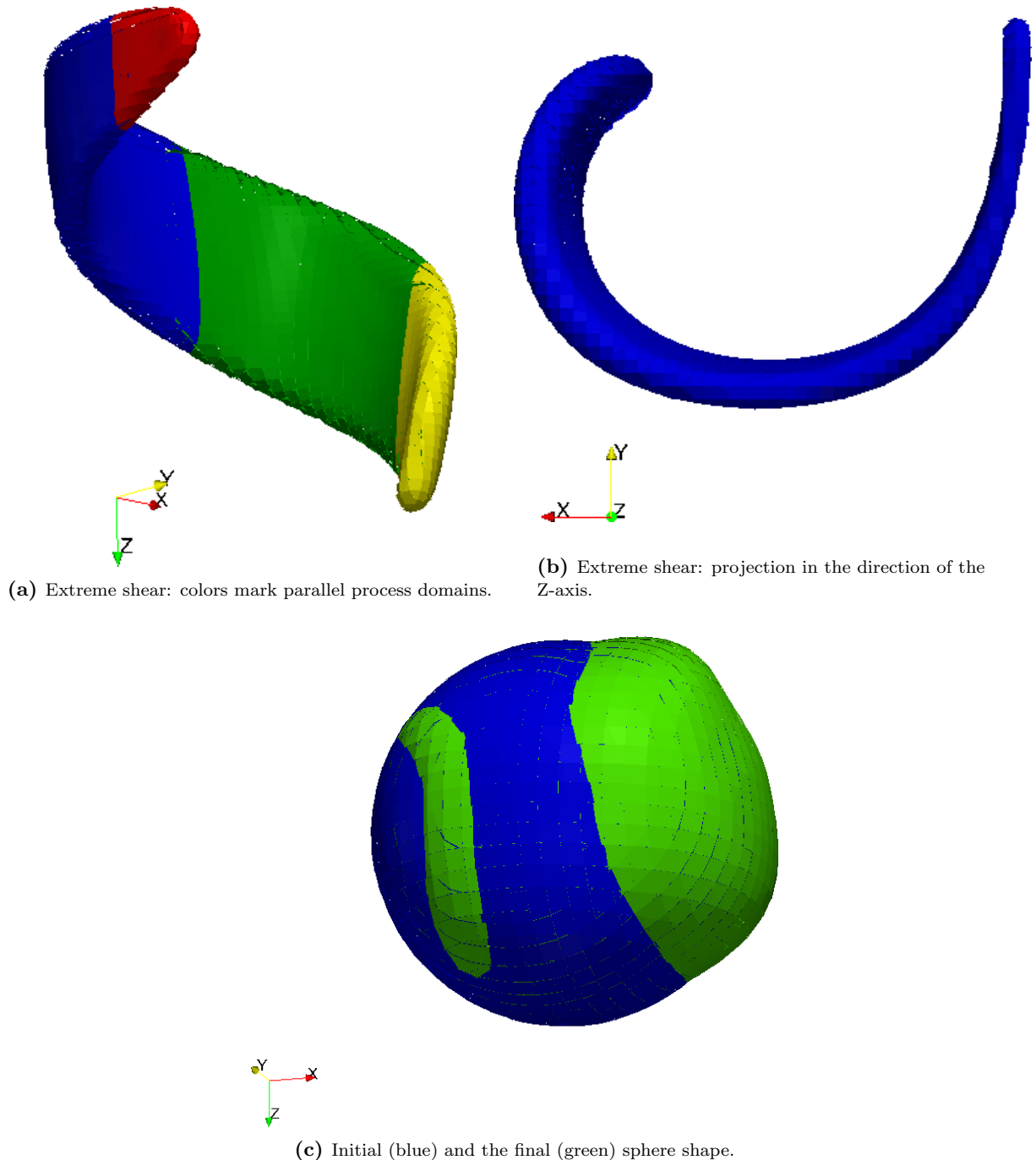


Figure 17. Shear test case on a mesh with 64^3 volumes.

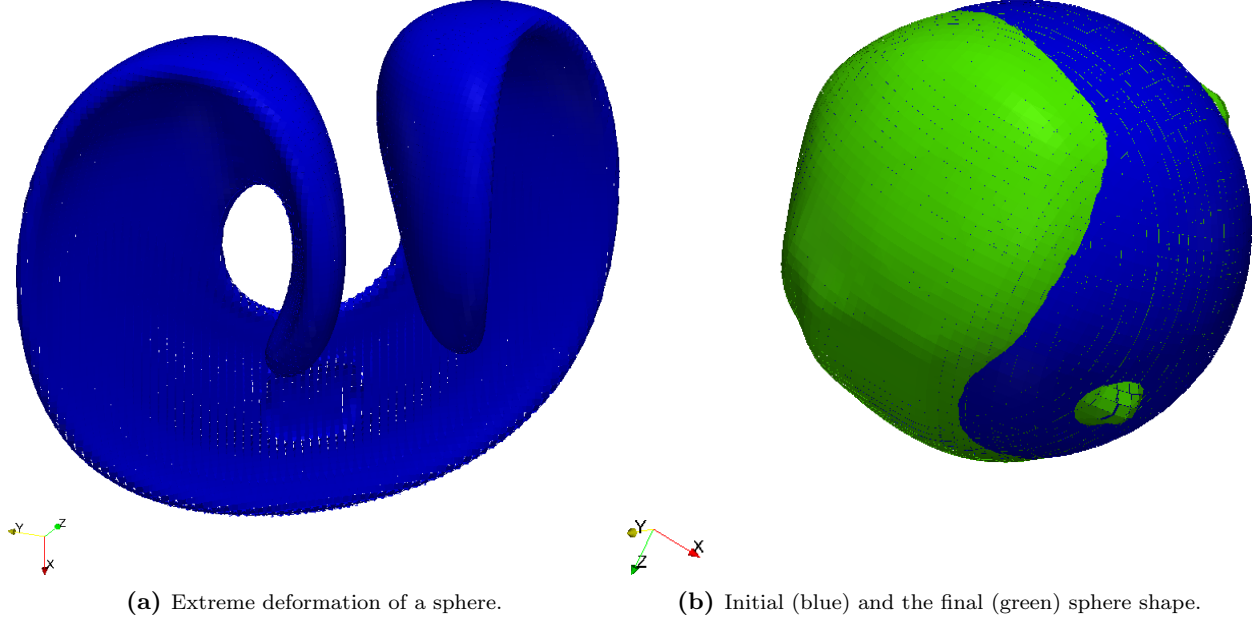
becomes extended into a very narrow filament. When the thickness of the layer approaches the cell size, the gradient calculation of the Young's reconstruction method is not accurate enough to stabilize the orientation of the interface normal. This is a common issue of the geometrical VoF method and a detailed description is provided by Černe et al. (2002). Two solutions may be applied in this case: a higher order reconstruction and/or local dynamic AMR. A higher order reconstruction method usually involves optimization of the interface normal orientation, which brings additional computational cost to the overall algorithm. On the other hand, the local dynamic AMR increases the accuracy of both the geometrical advection and the flow solution. The *locally increased mesh density* provided by local dynamic AMR will enable the geometrical algorithm to resolve very thin filaments, as well as the boundary layer surrounding the interface, while keeping a *low overall number of cells* in the mesh, thus increasing the overall efficiency of the solution.

4.3. Results using local adaptive AMR.

4.3.1. *Reconstruction.* To emphasize the advantages of basing our developments on an arbitrary unstructured mesh, we have chosen a reconstruction verification case involving a complex geometry. Arbitrarily, a geometry has been chosen consisting of a head part of a helical transmission gear for which the mesh

Table 4. Advection errors of deformation test case.

Number of volumes	16^3	32^3	64^3	128^3
Courant number				
0.1	1.34430e-02	7.776114e-03	1.53454e-03	8.09107e-04
0.5	1.48808e-02	8.157570e-03	2.53035e-03	1.30304e-03
0.75	1.58007e-02	8.978900e-03	3.17220e-03	1.58943e-03

**Figure 18.** Deformation test case on a mesh with 128^3 volumes.**Table 5.** Reconstruction data with local dynamic AMR.

Refinement level	0	1	2	3	4
E_{vsd}	5.36139e-06	3.79479e-06	1.37713e-06	3.85176e-07	1.27413e-07
E_{vsd} order of convergence	n/a	0.49	1.46	1.83	1.59
Normalized number of polygons	1	3.81	16	65.35	315
Normalized CPU time	1	1.17	2	6	22.67

was automatically generated. Clearly, this choice of the interface geometry is artificial, however it shows that arbitrary complexity of the interface reconstruction can be fully resolved with very little computational overhead using local dynamic AMR on unstructured hexahedral meshes, even with a geometrically first order convergent reconstruction algorithm.

Figure 19a shows the prescribed interface in the form of a helical gear (input mesh). The interface reconstructed with a refinement level of 4 is shown in the front view in Figure 19b and from the back view in Figure 19c. The background mesh of together with the refinement layers are visible in Figure 19d. Note that the initial mesh is very coarse; the length scale of a cell is in the order of magnitude of the width of the gear.

Table 5 contains the volume of symmetric difference error E_{vsd} , order of error convergence, as well as normalized CPU time and the normalized number of interface polygons with increasing level of mesh refinement. The small order of convergence observed initially for the refinement level 1 comes from the fact that the interface is severely under-resolved on the initial very coarse mesh. Once the local refinement reaches the cell length scale that is enough to sufficiently resolve the curvature of the interface, the convergence of the error increases significantly, which is expected for the geometrically first order convergent Youngs reconstruction algorithm. With further local mesh refinement the order of convergence of the E_{vsd} error stabilizes.

The CPU time increases almost linearly with the increase in the number of interface polygons, thus defining the overall reconstruction algorithm linear in complexity $O(N_{polygons})$. This linear relationship is visualized in Figure 20 in the form of a diagram.

4.3.2. *Advection.* In (Marić, Marschall, and Bothe, 2013) we have presented the results for the shear test case together with local dynamic AMR to verify the geometrical mapping algorithm. Table 6 holds an

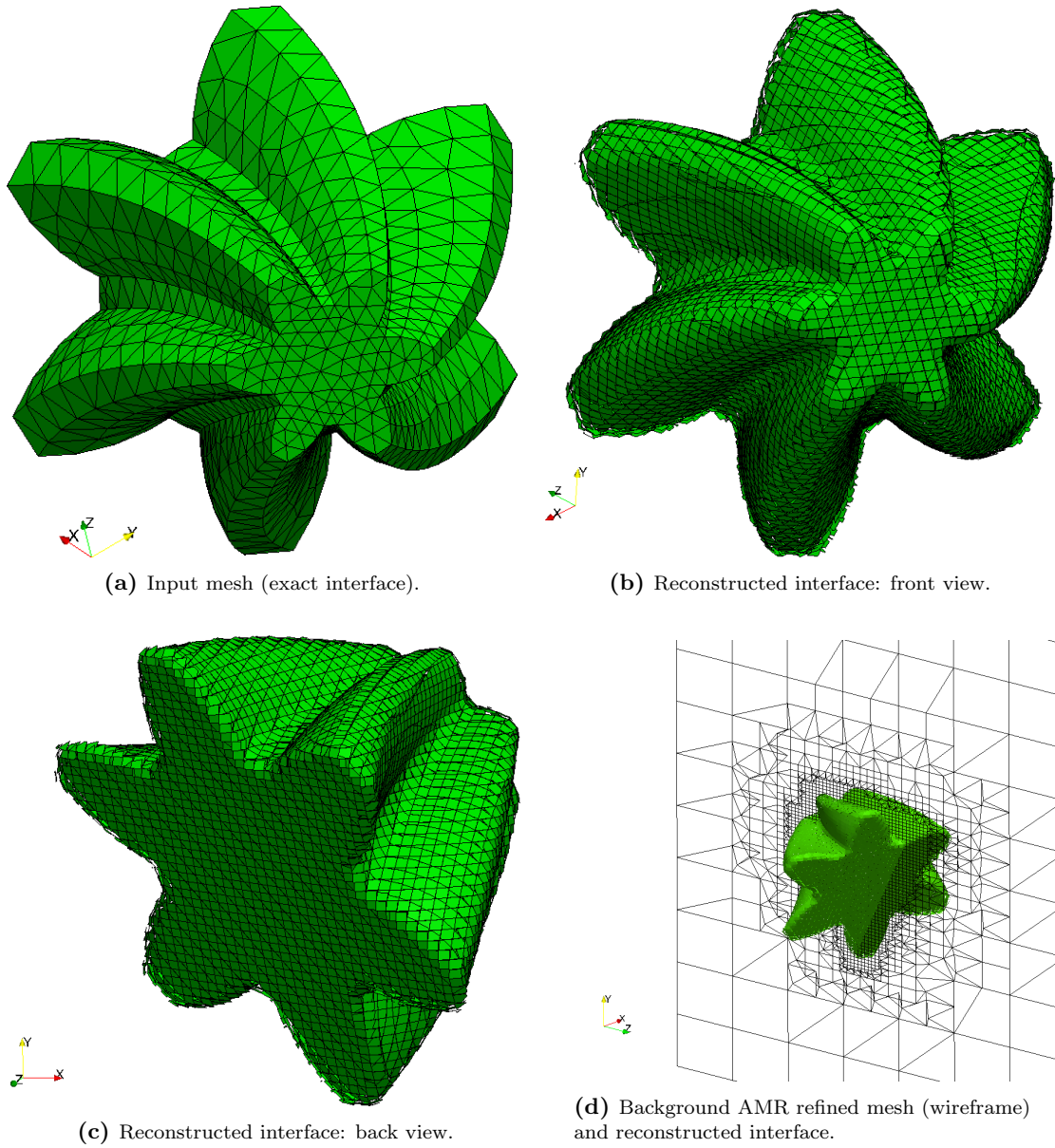


Figure 19. Illustration of capability to reconstruct complex interface geometries: Interface reconstruction for a helical gear geometry using local dynamic AMR.

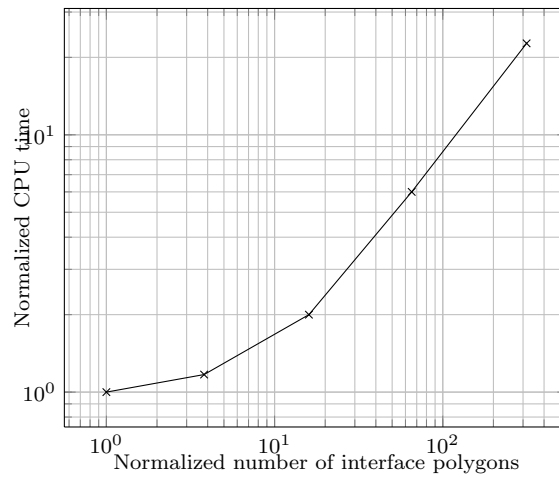
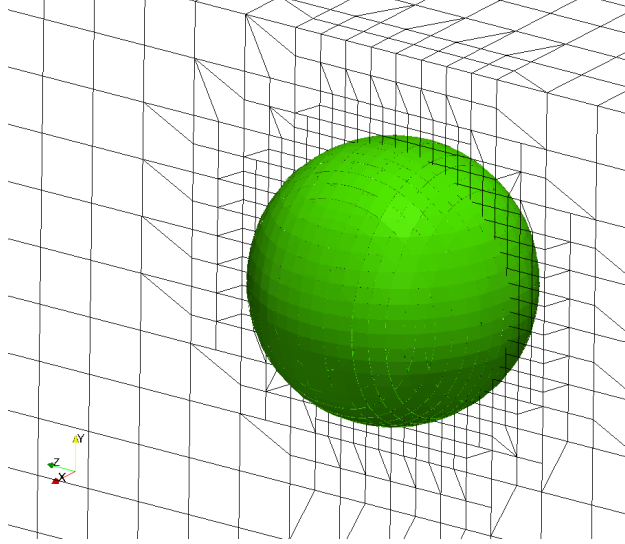


Figure 20. Linear dependency of the CPU time with respect to the number of interface polygons.

Table 6. Shear case data with local dynamic AMR.

Refinement level	1	2	3
E_{vsd}	5.8131E-003	2.7268E-003	1.11965E-003
E_{vsd} order of convergence	0.94	1.09	1.28
Normalized CPU time	0.83	0.71	0.58

**Figure 21.** Final sphere shape for a rotation case using local dynamic AMR with level 2 refinement.

excerpt of the solution results for this test case. The results of the shear advection executed together with the local dynamic AMR on an initial mesh of 16^3 volumes are consistent with the results obtained for the corresponding uniformly refined meshes with densities defined by the finest refinement level. The normalized CPU time with respect to the corresponding uniform shear test case shows the benefit of local dynamic AMR when it comes to the computational cost. To obtain the magnitude of the volume of symmetric error E_{vsd} corresponding to the mesh of 128^3 volumes (refinement level 3), only 58% of the CPU time is required. Further speedup is to be achieved by refactoring and optimization of the geometrical library. Figure 21 shows the final result of the rotation test case with local dynamic AMR (level 2 refinement).

5. Summary & Conclusions

We provide considerable detail on the characteristics and fundamental steps of method development of a novel geometrical unsplit VoF algorithm for arbitrary unstructured meshes. Our algorithm has shown to produce a bounded volume fraction field; moreover, it is mass conservative and robust, even though its advection part is based on a discrete Lagrangian flow map (velocities in mesh points), which has been reported to be unfeasible in literature so far.

The method's advection algorithm – besides its use of an unique discrete Lagrangian flow map – essentially comprises of a novel flux correction algorithm and narrow band computation: a fast iterative flux correction algorithm was implemented as well as an efficient narrow band computation based exclusively on the volume fraction field. This has been accomplished without introducing additional data structures and related algorithms required to update the narrow band as the interface moves. The key feature of the reconstruction algorithm is its accurate Node Averaged Gauss method used for calculating the phase fraction gradient, which results in lowest reconstruction errors reported so far for unstructured meshes.

The implementation of the geometrical intersection algorithms used both for reconstruction and advection is completely general, which makes the overall framework applicable to arbitrary cell types. However, the results show the algorithm to be more accurate on unstructured hexahedral meshes than on tetrahedral meshes. In order to obtain more accurate solutions on a tetrahedral mesh, higher order reconstruction and/or advection algorithms will be required, which is to be expected. To increase the overall accuracy on hexahedral meshes, we have extended the local dynamic Adaptive Mesh Refinement (AMR) engine in OpenFOAM and implemented a geometrical mapping algorithm for the volume fraction field. Results obtained using the adaptive geometrical VoF algorithm are promising and are showing expected behaviour in absolute error values as well as error convergence with a low computational overhead when compared to static mesh cases.

The implementation of the geometrical library and the client simulation applications was done in a modular way using a policy based design in the C++ programming language, allowing for straightforward future extensions, if proven to be necessary. Our VoF algorithm is fully parallelized using the domain decomposition approach and is developed such that it is fully dimension agnostic following the design of the OpenFOAM library, which means that the transport automatically supports both two and three dimensional computation. The results are based on the majority of the standard established test cases for verification and validation of VoF algorithms and show that the new geometrical VoF algorithm delivers accurate and reliable results on unstructured meshes, even for large Courant numbers and complex velocity fields.

Our further research is directed towards the coupling of the geometrical VoF algorithm with the pseudo-staggered flow solution algorithms in OpenFOAM on arbitrary unstructured meshes. Another point of interest related to a geometrically transported volume fraction field is the balancing of interfacial forces which will enable simulations of surface-tension dominated flows in flow domains of arbitrary geometrical complexity.

References

- Agbaglah, G., Delaux, S., Fuster, D., Hoepffner, J., Josserand, C., Popinet, S., Ray, P., Scardovelli, R., Zaleski, S., 2011. Parallel simulation of multiphase flows using octree adaptivity and the Volume-Of-Fluid method. *Comptes Rendus Mecanique* 339 (2-3), 194 – 207, high Performance Computing.
- Ahn, H., Shashkov, M., 2008. Geometric Algorithms for 3d Interface Reconstruction. In: Brewer, M. L., Marcum, D. (Eds.), *Proceedings of the 16th International Meshing Roundtable*. Springer Berlin Heidelberg, pp. 405–422.
- Ahn, H. T., Shashkov, M., 2007. Multi-material interface reconstruction on generalized polyhedral meshes. *J. Comput. Phys.* 226 (2), 2096 – 2132.
- Ahn, H. T., Shashkov, M., 2009. Adaptive Moment-Of-Fluid method. *J. Comput. Phys.* 228 (8), 2792 – 2821.
- Aulisa, E., Manservigi, S., Scardovelli, R., Zaleski, S., 2007. Interface reconstruction with least-squares fit and split advection in three-dimensional Cartesian geometry. *J. Comput. Phys.* 225 (2), 2301 – 2319.
- Brent, R. P., 1971. An algorithm with guaranteed convergence for finding a zero of a function. *Computer J.* 14, 422–425.
- Chenadec, V. L., Pitsch, H., 2013. A 3D unsplit forward/backward Volume-Of-Fluid approach and coupling to the Level Set Method. *J. Comput. Phys.* 233 (0), 10–33.
- Correa, C., Hero, R., Ma, K.-L., march 2011. A comparison of gradient estimation methods for volume rendering on unstructured meshes. *Visualization and Computer Graphics, IEEE Transactions on* 17 (3), 305 – 319.
- De Berg, M., Cheong, O., van Kreveld, M., 2008. *Computational Geometry: Algorithms and Applications*. Springer.
- DeBar, R., 1974. Fundamentals of the KRAKEN code. [Eulerian hydrodynamics code for compressible nonviscous flow of several fluids in two-dimensional (axially symmetric) region]. Tech. rep., California Univ., Livermore (USA). Lawrence Livermore Lab.
- Dyadechko, V., Shashkov, M., 2005. Moment-Of-Fluid interface reconstruction. Tech. rep., Los Alamos National Laboratory, Oct 2005. Available online at <http://math.lanl.gov/vdyadechko/doc/2005-mof.pdf>.
- Fuster, D., Agbaglah, G., Josserand, C., Popinet, S., Zaleski, S., 2009. Numerical simulation of droplets, bubbles and waves: state of the art. *Fluid Dynamics Research* 41 (6), 065001.
- Gabriel, E., Fagg, G. E., Bosilca, G., Angskun, T., Dongarra, J. J., Squyres, J. M., Sahay, V., Kambadur, P., Barrett, B., Lumsdaine, A., Castain, R. H., Daniel, D. J., Graham, R. L., Woodall, T. S., September 2004. Open MPI: Goals, Concept, and Design of a Next Generation MPI implementation. In: *Proceedings, 11th European PVM/MPI Users' Group Meeting*. Budapest, Hungary, pp. 97–104.
- Harvie, D. J. E., Fletcher, D. F., 2000. A new Volume of Fluid advection algorithm: The Stream Scheme. *J. Comput. Phys.* 162 (1), 1 – 32.
- Hernández, J., López, J., Gómez, P., Zanzi, C., Faura, F., 2008. A new Volume Of Fluid method in three dimensions: Part I: Multidimensional advection method with face-matched flux polyhedra. *Int. J. Numer. Meth. Fluids* 58 (8), 897–921.
- Ivey, C., Moin, P., 2012. Conservative Volume Of Fluid advection method on unstructured grids in three dimensions. *Center for Turbulence Research Annual Research Briefs*, 179-192.
- Jasak, H., Jemcov, A., Ž. Tuković, September 19-21 2007. OpenFOAM: A C++ library for complex physics simulations. In: *International Workshop on Coupled Methods in Numerical Dynamics IUC*, Dubrovnik, Croatia.
- Jófre, L., Lehmkuhl, O., Castro, J., Oliva, A., 2010. A PLIC-VOF implementation on parallel 3D unstructured meshes. In: *V European Conference on Computational Fluid Dynamics, ECCOMAS*.

- Kothe, D. B., Rider, W., Mosso, S. J., Brock, J. S., Hochstein, J. I., 1996. Volume Tracking of interfaces having surface tension in two and three dimensions. In: AIAA Meeting Proceedings 1996, AIAA Paper 96-0859. American Institute of Aeronautics and Astronautics.
- Kothe, D. B., Williams, M. W., Lam, K. L., Korzekwa, D. R., Tubesing, P. K., 1999. A second-order accurate, linearity-preserving Volume Tracking algorithm for free surface flows on 3-D unstructured meshes. In: Proceedings of the 3rd ASME/JSME. pp. 99–7109.
- Liović, P., Rudman, M., Liow, J.-L., Lakehal, D., Kothe, D., 2006. A 3D unsplit-advection volume tracking algorithm with planarity-preserving interface reconstruction. *Computers & Fluids* 35 (10), 1011 – 1032.
- López, J., Hernández, J., Gómez, P., Faura, F., 2004. A Volume Of Fluid method based on multidimensional advection and spline interface reconstruction. *Journal of Computational Physics* 195 (2), 718 – 742.
- López, J., Zanzi, C., Gómez, P., Faura, F., Hernández, J., 2008. A new Volume Of Fluid method in three dimensions - Part II: Piecewise-planar interface reconstruction with cubic-Bezier fit. *Int. J. Numer. Meth. Fluids* 58 (8), 923–944.
- Marić, T., Marschall, H., Bothe, D., May 2013. On the Adaptive Mesh Refinement for a 3D geometrical Volume of Fluid transport algorithm on unstructured meshes using OpenFOAM. In: Proceedings, International Conference on Multiphase Flows (ICMF). Jeju, Republic of Korea.
- Mavriplis, D. J., 2003. Revisiting the least-squares procedure for gradient reconstruction on unstructured meshes. Tech. rep., National Institute of Aerospace, Hampton, Virginia.
- Mencinger, J., Žun, I., 2011. A PLIC-VOF method suited for adaptive moving grids. *J. Comput. Phys.* 230 (3), 644 – 663.
- Mosso, S., Garasi, C., Drake, R., 2009. A smoothed two- and three-dimensional interface reconstruction method. *Computing and Visualization in Science* 12, 365–381.
- Mosso, S. J., Swartz, B. K., Kothe, D. B., Ferrell, R. C., 1996. A parallel, Volume-Tracking algorithm for unstructured meshes. In: Proceedings of Parallel CFD 96’.
- Noh, W., Woodward, P., 1976. Slic (Simple Line Interface Calculation). In: van de Vooren, A., Zandbergen, P. (Eds.), Proceedings of the Fifth International Conference on Numerical Methods in Fluid Dynamics June 28 July 2, 1976 Twente University, Enschede. Vol. 59 of Lecture Notes in Physics. Springer Berlin / Heidelberg, pp. 330–340.
- Parker, B., Youngs, D., 1992. Two and three dimensional Eulerian simulation of fluid flow with material interfaces. Tech. rep., Tech. Report 01/92, UK Atomic Weapons Establishment.
- Popinet, S., 2003. Gerris: A tree-based adaptive solver for the incompressible Euler equations in complex geometries. *J. Comput. Phys.* 190 (2), 572 – 600.
- Popinet, S., 2009. An accurate adaptive solver for surface-tension-driven interfacial flows. *J. Comput. Phys.* 228 (16), 5838 – 5866.
- Puckett, E. G., 1991. A Volume-Of-Fluid Interface Tracking algorithm with applications to computing shock wave refraction. In: Proceedings of the Fourth International Symposium on Computational Fluid Dynamics.
- Rider, W. J., Kothe, D. B., 1998. Reconstructing volume tracking. *J. Comput. Phys.* 141 (2), 112 – 152.
- Scardovelli, R., Zaleski, S., 1999. Direct numerical simulation of free-surface and interfacial flow. *Annu. Rev. Fluid. Mech.* 31 (1), 567–603.
- Scardovelli, R., Zaleski, S., 2000. Analytical relations connecting linear interfaces and volume fractions in rectangular grids. *J. Comput. Phys.* 164 (1), 228 – 237.
- Scardovelli, R., Zaleski, S., 2003. Interface reconstruction with least-square fit and split Eulerian-Lagrangian advection. *Int. J. Numer. Meth. Fluids* 41 (3), 251–274.
- Schneider, P. J., Eberly, D., 2002. *Geometric Tools for Computer Graphics*. Elsevier Science Inc., New York, NY, USA.
- Tryggvason, G., Scardovelli, R., Zaleski, S., 2011. *Direct Numerical Simulations of Gas-Liquid Multiphase Flows*. Cambridge University Press.
- Černe, G., Petelin, S., Tiselj, I., 2002. Numerical errors of the Volume-Of-Fluid interface tracking algorithm. *Int. J. Numer. Meth. Fluids* 38 (4), 329–350.
- Weller, H. G., Tabor, G., Jasak, H., Fureby, C., 1998. A tensorial approach to Computational Continuum Mechanics using object oriented techniques. *Comput. Phys.* 12, 620–631.
- Weymouth, G., Yue, D., 2010. Conservative Volume-Of-Fluid method for free-surface simulations on Cartesian grids. *J. Comput. Phys.* 229 (8), 2853–2865.

MATHEMATICAL MODELING AND ANALYSIS GROUP, CENTER OF SMART INTERFACES, TECHNISCHE UNIVERSITÄT DARMSTADT,
GERMANY
E-mail address: `maric@csi.tu-darmstadt.de`

MATHEMATICAL MODELING AND ANALYSIS GROUP, CENTER OF SMART INTERFACES, TECHNISCHE UNIVERSITÄT DARMSTADT,
GERMANY
E-mail address: `marschall@csi.tu-darmstadt.de`

MATHEMATICAL MODELING AND ANALYSIS GROUP, CENTER OF SMART INTERFACES, TECHNISCHE UNIVERSITÄT DARMSTADT,
GERMANY
E-mail address: `bothe@csi.tu-darmstadt.de`